

Exploring the extended density dependent Skyrme effective forces for normal and isospin-rich nuclei to neutron stars

B. K. Agrawal¹, Shashi K. Dhiman^{2,3} and Raj Kumar³

¹*Saha Institute of Nuclear Physics, Kolkata - 700064, India*

²*School of Physical Sciences, Jawaharlal Nehru University, New Delhi 110067 India.*

³*Department of Physics, H.P. University, Shimla 171 005 India.*

Abstract

We parameterize the recently proposed generalized Skyrme effective force (GSEF) containing extended density dependence. The parameters of the GSEF are determined by the fit to several properties of the normal and isospin-rich nuclei. We also include in our fit a realistic equation of state for the pure neutron matter up to high densities so that the resulting Skyrme parameters can be suitably used to model the neutron star with the “canonical” mass ($\sim 1.4M_{\odot}$). For the appropriate comparison we generate a parameter set for the standard Skyrme effective force (SSEF) using exactly the same set of the data as employed to determine the parameters of the GSEF. We find that the GSEF yields larger values for the neutron skin thickness which are closer to the recent predictions based on the isospin diffusion data. The Skyrme parameters so obtained are employed to compute the strength function for the isoscalar giant monopole, dipole and quadrupole resonances. It is found that in the case of GSEF, due to the the larger value of the nucleon effective mass the values of centroid energies for the isoscalar giant resonances are in better agreement with the corresponding experimental data in comparison to those obtained using the SSEF. We also present results for some of the key properties associated with the neutron star of “canonical” mass and for the one with the maximum mass.

PACS numbers: 21.10.-k,21.65+f,24.30.Cz,21.60jz,26.60.+c

I. INTRODUCTION

The density dependent Skyrme type effective nucleon-nucleon interaction [1] within the Hartree-Fock (HF) approximation has been one of the most successful and popular microscopic tools to describe the ground state properties of the finite nuclei as well as that of the symmetric nuclear and pure neutron matters. The pioneering work [2] of implementing the Skyrme type effective force having only a linear density dependence was carried out to reproduce the experimental data on the binding energy and charge rms radii. The linear density dependence gave rise to the value of nuclear matter incompressibility coefficient K_∞ in the range of 300 – 400 MeV which is much higher compared to the experimental value ~ 220 MeV. It was proposed in Ref. [3] that in order to obtain a reasonable value of K_∞ the linear density dependence in the Skyrme effective force must be modified to ρ^α with α lying in between $\frac{1}{3}$ to $\frac{2}{3}$. Since then, numerous attempts have been made to parameterize the standard Skyrme effective force (SSEF) which contains only a single density dependent term (e.g., see Ref. [4, 5, 6, 7, 8, 9, 10, 11, 12, 13]). Recently several parameter sets for the SSEF are obtained by fits to large set of data comprising the binding energy, charge rms radii and single-particle energies for the nuclei ranging from normal to isospin-rich ones. Further, the Skyrme parameters are constrained by demanding that the equation of state (EOS) for the pure neutron matter should be reasonable up to the densities relevant for studying the properties of neutron star [9, 12, 13].

Recently, studies involving the generalized Skyrme effective force (GSEF) have been revisited [14, 15, 16, 17]. Generalization of the Skyrme effective force can be realized by adding several density dependent terms to each of the three, namely, local, non-local and spin-orbit parts of the SSEF. The multi density-dependent terms used in Refs. [15, 16] are of the form $\rho^{\nu/3}$ with $\nu = 1, 2$, and 3 connected to the Fermi momentum (k_F) expansion of the Brueckner G matrix. Similar density dependence is also found in the energy density functional derived within the chiral perturbation theory containing the contributions from one and two pion exchange diagrams up to three-loops [18]. In Refs. [15, 16] the GSEF containing extended density dependence in the local part of the Skyrme interaction is used only to study the properties of nuclear matter. It is found that the extended density dependence gives rise to reasonable EOS for the infinite nuclear matter for any given asymmetry. It has been also demonstrated that unlike in the case of SSEF the value of K_∞ and the isoscalar

nucleon effective mass m^* can be determined independently using the GSEF. Thus, one may expect the GSEF to reproduce concurrently the experimental values for the K_∞ and the single-particle energies in nuclei. We would like to mention that some early attempts [19, 20, 21, 22] to generalize the density dependence of Skyrme type effective interaction were significantly different compared to the one proposed recently [15, 16]. In Ref. [22] the exponents of the density dependent terms are obtained by a fit to several nuclear observables. Moreover, most of these forces are plagued by an undesirable feature that they give collapse in the nuclear matter at high densities which leave them unsuitable for their use for the study of neutron star.

In the present paper we determine the parameters of the GSEF by the fit to a set of experimental data for the binding energies, charge rms radii, single particle energies and rms radii of valence neutron orbits. Our data set used in the fit consists of 13 spherical nuclei, namely, ^{16}O , ^{24}O , ^{40}Ca , ^{48}Ca , ^{48}Ni , ^{56}Ni , ^{68}Ni , ^{78}Ni , ^{88}Sr , ^{90}Zr , ^{100}Sn , ^{132}Sn and ^{208}Pb . We also fit the experimental data for the breathing mode energies for the ^{90}Zr , and ^{208}Pb nuclei. Further, we constrain the value of Skyrme parameters by including in the fit a realistic EOS for the pure neutron matter. The chi-square minimization, required to obtain the best fit parameters, is achieved by using the simulated annealing method (SAM) as recently implemented [13] to determine the parameters of the SSEF.

The present paper is organized as follows. In Sec. II we briefly outline the form of the GSEF and the corresponding energy density functional adopted in the present work. In this section, we also mention in short the strategies used to evaluate center of mass corrections to the binding energy and charge radii. In Sec. III we briefly describe a procedure for minimization of the χ^2 function based on the SAM and present the set of the experimental data along with the constraints used in the fit to determine the values of the Skyrme parameters. In the same section we list the values of the parameter sets for the GSEF and SSEF. In Sec. IV we present our results for the three different fits carried out in this work. We also present results for the isoscalar giant monopole, dipole and quadrupole resonances and some key properties of the neutron stars obtained using the newly generated parameter sets. Finally, in Sec. V we summarize our main results.

II. GENERALIZED SKYRME EFFECTIVE FORCE

The GSEF used in Refs. [15, 16] can be written as,

$$\begin{aligned}
V(\vec{r}_1, \vec{r}_2) &= t_0 (1 + x_0 P_\sigma) \delta(\vec{r}) \\
&+ \frac{1}{2} t_1 (1 + x_1 P_\sigma) \left[\delta(\vec{r}) \vec{P}'^2 + \vec{P}^2 \delta(\vec{r}) \right] \\
&+ t_2 (1 + x_2 P_\sigma) \vec{P}' \cdot \delta(\vec{r}) \vec{P} \\
&+ \sum_i t_{3i} \rho^{\alpha_i} (1 + x_{3i} P_\sigma) \delta(\vec{r}) \\
&+ i W_0 \vec{\sigma} \cdot \left[\vec{P}' \times \delta(\vec{r}) \vec{P} \right]
\end{aligned} \tag{1}$$

with $i = 1, 2, 3, \dots$ and $\alpha_i = i/3$. In Eq. (1), $\vec{r} = \vec{r}_1 - \vec{r}_2$, $\vec{P} = \frac{\vec{V}_1 - \vec{V}_2}{2i}$, \vec{P}' is complex conjugate of \vec{P} acting on the left and $\vec{\sigma} = \vec{\sigma}_1 + \vec{\sigma}_2$, $P_\sigma = \frac{1}{2} (1 + \vec{\sigma}_1 \cdot \vec{\sigma}_2)$. The SSEF can be obtained from Eq. (1) simply by setting $t_{3i} = 0$ for $i \neq 1$ and α_1 is normally taken to be less than unity. For instance, in the SIII force [23] α_1 is unity and for the SLy forces [9] $\alpha_1 = 1/6$ was used. It may be noted that we have considered the extended density dependence only for the local term in Eq. (1). However, on the same analogy the non-local and spin-orbit terms can also be extended to have density dependence.

The total energy E of the system is given by,

$$E = \int \mathcal{H}(r) d^3r \tag{2}$$

where, $\mathcal{H}(r)$ is the Skyrme energy density functional corresponding to Eq. (1) which under the time-reversal invariance is given by [2, 9],

$$\mathcal{H} = \mathcal{K} + \mathcal{H}_\delta + \mathcal{H}_\rho + \mathcal{H}_{\text{eff}} + \mathcal{H}_{\text{fin}} + \mathcal{H}_{\text{so}} + \mathcal{H}_{\text{sg}} + \mathcal{H}_{\text{Coul}} \tag{3}$$

where, $\mathcal{K} = \frac{\hbar^2}{2m} \tau$ is the kinetic energy term, \mathcal{H}_δ is the zero-range term, \mathcal{H}_ρ the density dependent term, \mathcal{H}_{eff} an effective-mass term, \mathcal{H}_{fin} a finite-range term, \mathcal{H}_{so} a spin-orbit term, \mathcal{H}_{sg} a term due to tensor coupling with spin and gradient and $\mathcal{H}_{\text{Coul}}$ is the contribution to the energy density for protons due to the Coulomb interaction. For the Skyrme interaction of Eq. (1), we have,

$$\mathcal{H}_\delta = \frac{1}{4} t_0 \left[(2 + x_0) \rho^2 - (2x_0 + 1) (\rho_p^2 + \rho_n^2) \right], \tag{4}$$

$$\mathcal{H}_\rho = \frac{1}{4} \sum_i t_{3i} \rho^{\alpha_i} \left[(2 + x_{3i}) \rho^2 - (2x_{3i} + 1) (\rho_p^2 + \rho_n^2) \right], \tag{5}$$

$$\mathcal{H}_{\text{eff}} = \frac{1}{8} [t_1(2 + x_1) + t_2(2 + x_2)] \tau \rho + \frac{1}{8} [t_2(2x_2 + 1) - t_1(2x_1 + 1)] (\tau_p \rho_p + \tau_n \rho_n), \quad (6)$$

$$\begin{aligned} \mathcal{H}_{\text{fin}} &= \frac{1}{32} [3t_1(2 + x_1) - t_2(2 + x_2)] (\nabla \rho)^2 \\ &\quad - \frac{1}{32} [3t_1(2x_1 + 1) + t_2(2x_2 + 1)] [(\nabla \rho_p)^2 + (\nabla \rho_n)^2], \end{aligned} \quad (7)$$

$$\mathcal{H}_{\text{so}} = \frac{W_0}{2} [\mathbf{J} \cdot \nabla \rho + \mathbf{J}_p \cdot \nabla \rho_p + \mathbf{J}_n \cdot \nabla \rho_n], \quad (8)$$

$$\mathcal{H}_{\text{sg}} = -\frac{1}{16} (t_1 x_1 + t_2 x_2) \mathbf{J}^2 + \frac{1}{16} (t_1 - t_2) [\mathbf{J}_p^2 + \mathbf{J}_n^2], \quad (9)$$

$$\mathcal{H}_{\text{Coul}}(r) = \frac{1}{2} e^2 \rho_p(r) \int \frac{\rho_p(r') d^3 r'}{|\mathbf{r} - \mathbf{r}'|} - \frac{3}{4} e^2 \rho_p(r) \left(\frac{3\rho_p(r)}{\pi} \right)^{1/3}. \quad (10)$$

Here, $\rho = \rho_p + \rho_n$, $\tau = \tau_p + \tau_n$, and $\mathbf{J} = \mathbf{J}_p + \mathbf{J}_n$ are the particle number density, kinetic energy density and spin density with p and n denoting the protons and neutrons, respectively. We have used the value of $\hbar^2/2m = 20.734 \text{ MeV fm}^2$ in our calculations. We would like to emphasize that we have included the contributions from the spin-density term as given by Eq. (9) so that the corresponding contributions can be considered consistently in evaluating the Landau parameter G'_0 [24]. Although the contributions from Eq. (9) to the binding energy and charge radii are not very significant, but they may contribute significantly to the value of the Landau parameter G'_0 .

The single-particle wave functions ϕ_i and corresponding single-particle energies ε_i are obtained by solving the HF equations given by,

$$\left[-\vec{\nabla} \frac{\hbar^2}{2m_q^*(\mathbf{r})} \cdot \vec{\nabla} + U_q(\mathbf{r}) - i\vec{W}_q(\mathbf{r}) \cdot (\vec{\nabla} \times \vec{\sigma}) \right] \phi_i(\mathbf{r}, q) = \varepsilon_i \phi_i(\mathbf{r}, q), \quad (11)$$

where, m_q^* is the effective nucleon mass, U_q and W_q are the central and spin-orbit parts of the mean field potentials. The expressions for the m_q^* and W_q can be found in Ref. [9]. The

expression for U_q is given as,

$$\begin{aligned}
U_q(\mathbf{r}) = & \frac{1}{2}t_0[(2+x_0)\rho(\mathbf{r}) - (1+2x_0)\rho_q(\mathbf{r})] \\
& + \frac{1}{8}[t_1(2+x_1) + t_2(2+x_2)]\tau(\mathbf{r}) - \frac{1}{8}[t_1(1+2x_1) - t_2(1+2x_2)]\tau_q(\mathbf{r}) \\
& + \frac{1}{4}\sum_i t_{3i} \left\{ (2+x_3)(2+\alpha_i)\rho^{\alpha_i+1}(\mathbf{r}) - (1+2x_3) [\alpha_i\rho^{\alpha_i-1}(\mathbf{r})(\rho_p^2(\mathbf{r}) + \rho_n^2(\mathbf{r})) + 2\rho^{\alpha_i}(\mathbf{r})\rho_q] \right\} \\
& - \frac{1}{16}[3t_1(2+x_1) - t_2(2+x_2)]\nabla^2\rho(\mathbf{r}) \\
& + \frac{1}{16}[3t_1(1+2x_1) + t_2(1+2x_2)]\nabla^2\rho_q(\mathbf{r}) \\
& - \frac{1}{2}W_0 \left(\vec{\nabla} \cdot \vec{J} + \vec{\nabla} \cdot \vec{J}_q \right) + \delta_{q,p} V_{\text{Coul}}(\mathbf{r}), \tag{12}
\end{aligned}$$

where, $q = p, n$.

To this end we briefly outline the corrections made to the HF results for the binding energies and charge rms radii arising from various effects as follows. The center of mass (CM) corrections to the binding energies and charge rms radii are made using simple prescriptions discussed in Ref. [13, 25]. We also consider the corrections to the charge rms radii due to the spin-orbit effect as well as the charge distributions of the neutron and proton [9, 26]. The contribution from the Coulomb exchange term in Eq. (10) is dropped in order to compensate for the effects of the long-range correlations [27] on the Coulomb displacement energy (CDE) in mirror nuclei. We also add the modified Wigner term [28],

$$E_w = V_w \exp \left\{ -\lambda \left(\frac{N-Z}{A} \right)^2 \right\} + V_{w'} |N-Z| \exp \left\{ -\left(\frac{A}{A_0} \right)^2 \right\} \tag{13}$$

to the binding energy. Values of the parameters V_w , $V_{w'}$, λ and A_0 are determined by the fit.

III. PARAMETERIZATION OF THE GENERALIZED SKYRME EFFECTIVE FORCE

The parameters of the GSEF can be determined by minimizing the value of χ^2 which is given as,

$$\chi^2 = \frac{1}{N_d - N_p} \sum_{i=1}^{N_d} \left(\frac{M_i^{exp} - M_i^{th}}{\sigma_i} \right)^2 \tag{14}$$

where, N_d is the number of experimental data points and N_p the number of fitted parameters. The σ_i stands for theoretical error and M_i^{exp} and M_i^{th} are the experimental and

the corresponding theoretical values, respectively, for a given observable. The values of χ^2 depends on the Skyrme parameters, since, the M_i^{th} in Eq. (14) is calculated using the HF approach with a Skyrme type effective nucleon-nucleon interaction. Thus, it is clear that the best fit parameters can be obtained using an appropriate method for the χ^2 minimization together with a set of experimental data. We briefly describe below the SAM for the χ^2 minimization and the set of experimental data selected to obtain the best fit parameters.

A. SAM algorithm for χ^2 minimization

The concept of SAM is based on the manner in which liquids freeze or metals recrystallize in the process of annealing. In an annealing process a metal, initially at high temperature and disordered, slowly cools so that the system at any time is in a thermodynamic equilibrium. As cooling proceeds, the system becomes more ordered and approaches a frozen ground state at zero temperature. The SAM is an elegant technique for optimization problems of large scale, in particular, where a desired global extremum is hidden among many local extrema. This method has been found to be an extremely useful tool for a wide variety of minimization problems of large non-linear systems in many different areas of science (e.g., see Refs. [29, 30, 31]). Very recently [32, 33], the SAM was used to generate some initial trial parameter sets for the point coupling variant of the relativistic mean field model.

In Ref. [13] we have implemented the SAM to the problem of searching the global minimum in the hypersurface of χ^2 function as defined by Eq. (14). Here too we shall use the SAM to determine the parameters of the GSEF. In the SAM one needs to specify the appropriate annealing schedule together with the parameter space (i.e., the range of the values of the parameters) in which the best fit parameters are to be searched. Similar to that in Ref. [13], in the present work we have employed a moderately faster annealing schedule such as Cauchy annealing schedule given by,

$$T(k) = T_i/k \tag{15}$$

where, T_i is the initial value of the control parameter (also viewed as effective temperature) and $T(k)$ with $k = 1, 2, 3, \dots$ is the control parameter at k -th step. The value of k is increased by unity after $100N_p$ reconfigurations or $10N_p$ successful reconfigurations whichever occurs first. The value of T_i is taken to be 1.25 which is same as that used in Ref. [13]. We keep

on reducing the value of the control parameter using Eq. (15) in the subsequent steps until the effort to reduce the value of χ^2 further becomes sufficiently discouraging. In Ref. [13] instead of the range of the values of the Skyrme parameters we used range of the values of the quantities associated with the symmetric nuclear matter. Since, it was possible to identify the number of nuclear matter quantities linearly related to the equal number of parameters for the SSEF. But, in the case of GSEF the numbers of parameters are larger and we shall define the parameter space directly in terms of the range of the values each of the Skyrme parameter can take. In Table I we give the lower and upper limits for the values of the Skyrme parameters denoted by \mathbf{v}_0 and \mathbf{v}_1 , respectively. The quantity \mathbf{d} in the penultimate column denotes the maximum displacement allowed in a single step for a given Skyrme parameter during the reconfiguration process (see also Ref. [13] for detail). The last column labeled as \mathbf{v}_{in} contains initial values for the Skyrme parameters used as a starting point for the SAM. These values for the parameters are the same as that for SGI force [4] which has $\rho^{1/3}$ density dependence. The parameters of the Wigner term (Eq. 13) are taken from Ref. [28]. The lower and upper limits and the initial values for the parameters α_i are taken to be the same indicating that these parameters are kept fixed during the χ^2 minimization.

B. Data used in the fitting procedure

We now summarize our selection of data and corresponding theoretical errors adopted in the fitting procedure. In Table II we list our choice of the data along with their sources [34, 35, 36, 37, 38, 39, 40, 41, 42]. It must be noted that in addition to the data on the binding energy, charge radii and single particle energies, the values of the Skyrme parameters are further constrained by including in the fit the experimental data for the radii of valence neutron orbits, breathing mode energies together with a realistic EOS for the pure neutron matter upto the densities ($\sim 0.8 \text{ fm}^{-3}$) relevant for the study of neutron stars. For the binding energy we use in our fit the error of 1.0 MeV except for the ^{100}Sn nucleus. The binding energy for the ^{100}Sn nucleus is determined from systematics and are expected to have large errors. Thus, we assign it a theoretical error of 2.0 MeV. For the charge rms radii we use the theoretical error of 0.02 fm except for the case of ^{56}Ni nucleus. The charge rms radius for the ^{56}Ni nucleus is obtained from systematics and we use the theoretical error

of 0.04 fm. For the rms radii of the valence neutron orbits in ^{17}O and ^{41}Ca nuclei we use $r_v(\nu 1d_{5/2}) = 3.36$ fm and $r_v(\nu 1f_{7/2}) = 3.99$ fm, [37, 38] respectively. The theoretical error taken for the rms radii for the valence neutron orbits is 0.06 fm. We must point out that the choice of the theoretical error on the rms radii for the valence neutron orbits is due to the large uncertainties associated with their extraction from the experimental measurements. To be consistent with the way these valence neutron radii are determined, we do not include the center of mass correction to these data. For each of the 22 single-particle (S-P) energies in the ^{208}Pb nucleus, we have used the theoretical error of 1.0 MeV in our fit. The experimental data for the breathing mode constrained energies E_0 included in our fit are 17.81, and 14.18 MeV for the ^{90}Zr and ^{208}Pb nuclei [41], respectively, with the theoretical error taken to be 0.5 MeV for the ^{90}Zr nucleus and 0.3 MeV for the ^{208}Pb nucleus. We also include in the fit the EOS for the pure neutron matter of a realistic UV14+UVII model [42]. We use 15 data points for the EOS corresponding to the densities up to $5\rho_0$. The theoretical error on each of these 15 data points are taken to be 2.0 MeV.

C. Parameters for the generalized Skyrme effective force

Following the fitting procedure described in Sec. III A together with the list of data given in Table II we have generated two different parameter sets for the GSEF. These parameter sets are given in Table III. The parameter set GSkI and GSkII are obtained as follows; GSkI includes the density dependent terms proportional to ρ^{α_i} with $\alpha_i = 1/3, 2/3$ and 1, whereas, GSkII force has only $\rho^{1/3}$ and $\rho^{2/3}$ density dependent terms. The exponents for the density dependence are taken to be 1/3 and 2/3 for the GSkII interaction due to the following reasons. The $\rho^{2/3}$ density dependence decouples the effective mass and the nuclear matter incompressibility coefficient [15]. On the otherhand, the SSEF favours the exponent of density dependence to lie in between $1/3 - 1/6$ in order to give an acceptable value for the nuclear matter incompressibility coefficient. In the last column of Table III we give the values of parameters corresponding to the SSEF [9]. We name this force as SSk which is obtained using the same set of data as those for the GSkI and GSkII forces. We shall see in the following section that the quality of the fit for the GSkI force is better in comparison to the ones obtained using GSkII and SSk forces. It can be seen from Eq. (1) that the density dependence in the GSkI force requires six parameters, namely, t_{3i} and x_{3i} with $i = 1, 2$ and

3, whereas, in the SSk force the density dependence is specified by three parameters, t_{31} , x_{31} and α_1 . Thus, fit to the GSEF considered here requires three additional parameters.

IV. RESULTS AND DISCUSSIONS

We generate the parameter sets GSkI and GSkII for the GSEF using the experimental data on the bulk properties for the nuclei ranging from the normal to isospin-rich ones. The values for the Skyrme parameters are further constrained by including in fit the experimental data on the breathing mode energies and a realistic EOS for the pure neutron matter. For the appropriate comparison we also obtain a parameter set named SSk for the SSEF using the same set of data as used to determine the parameters of the GSEF. The values of parameters for all the three forces in consideration are given in Table III. In the following subsections we shall present the results obtained using these three different parameter sets.

A. Infinite symmetric and asymmetric nuclear matter

In Table IV we give the values of various quantities associated with the symmetric nuclear matter at the saturation density obtained for GSkI, GSkII and SSk forces. We see that the values for all the quantities except for the m^* and

$$L = 3\rho \frac{dJ}{d\rho}, \quad (16)$$

given in Table IV are quite close to each other for all the three forces. The values of m^* and L for the GSkI and GSkII forces are little larger than that for the SSk force. The value of $m^* \sim 0.8m$ for the GSkI and GSkII forces is highly desirable in order to appropriately reproduce the location of the isoscalar giant quadrupole resonance [43]. Further, we shall see below that larger value of m^* gives rise to the single-particle energies which are in better agreement with the experimental data. The values of L at the saturation density obtained for the GSkI and GSkII forces in comparison to the one for the SSk force are in better agreement with the recently extracted value of $L = 88 \pm 25$ MeV [44].

We consider the behavior of the symmetry energy coefficient $J(\rho)$ for densities relevant to the study of neutron stars. It is well known [45, 46] that the values of $J(\rho)$ and the resulting EOS for the pure neutron matter at higher densities ($\rho > 2\rho_0$, $\rho_0 = 0.16 \text{ fm}^{-3}$) are crucial

in understanding the various properties of neutron star. For example, the proton fraction at any density depends strongly on the value of $J(\rho)$ at that density, which in turn affects the chemical compositions as well as the cooling mechanism of the neutron star [47]. Yet, no consensus is reached for the density dependence of $J(\rho)$. We display in Fig. 1, our results for the variation of the symmetry energy J as a function of the nuclear matter density ρ . We see that the value of J increases with density. The slope of $J(\rho)$ being positive upto $3\rho_0$ for GSkI, GSkII and SSk forces indicate that these interactions can be used to study the properties of the neutron star with masses around $1.4M_\odot$ [48]. In Fig. 2 we plot the EOS for the nuclear matter for various proton fraction ($Y_p = \rho_p/\rho$) as a function of density. The solid squares represent the EOS for the pure neutron matter (i.e., $Y_p = 0$) for a realistic UV14+UVII model [42]. It can be seen that the EOS for the pure neutron matter obtained using GSkI force is in better agreement with the one obtained for the UV14+UVII model.

B. Fit to the nuclear bulk properties

In Fig. 3 we present our results obtained using the GSkI, GSkII and SSk forces for the relatives errors in the values of total binding energies for the nuclei used in the fit. The rms error for the total binding energy are 1.18, 1.72 and 1.28 MeV for the GSkI, GSkII and SSk forces, respectively. Thus, We can say that the quality of the fit to the binding energies for the GSkI and SSk forces are more or less the same and they are much better than that for GSkII force. The binding energy difference $B(^{48}\text{Ca}) - B(^{48}\text{Ni}) = 66.82, 66.57$ and 66.95 MeV for the GSkI, GSkII and SSk interactions, respectively, compared to the experimental value of 68.85 MeV. The said difference for the SKX interaction [10] is 66.3 MeV which is about 0.5 MeV lower as compared to our present results. On the other hand, most of the Skyrme interactions which include the contribution from the exchange Coulomb term yield $B(^{48}\text{Ca}) - B(^{48}\text{Ni}) \approx 63$ MeV, which is about 6 MeV lower than the corresponding experimental value. To this end we would like to remark that the Wigner corrections (Eq. (13)) are more significant for the GSk forces as compared to the one for the SSk force. It may be verified by using the values of the Wigner parameters given in Table III that for the symmetric nuclei the Wigner correction is greater than 2.5 MeV for the GSk forces which is more than twice than that for the SSk force. Also for asymmetric nuclei we find that the GSk forces has larger Wigner corrections for the higher nuclei. For example, in case of ^{24}O

the Wigner correction is about 4.0(0.5) MeV for the GSk(SSk) forces. In Fig. 4 we present our results for the relative errors in the values of charge rms radii for the nuclei used in the fit. The rms error for the charge rms radii are 0.023, 0.026 and 0.021 fm for the GSkI, GSkII and SSk forces, respectively. The quality of fit for the charge rms radii is more or less same for all the three forces considered here.

In Fig. 5 we give the values for the single-particle energies for the ^{208}Pb nucleus used in the fits. We see that the values of the single-particle energies for the case of GSkI and GSkII forces are in slightly better agreement with the experimental data as compared to the ones obtained for the SSk force. This is mainly due to the weakening of the correlations between the effective mass m^* and the incompressibility coefficient K_∞ in the case of the GSEF [15, 16]. In Table V we present our results for the rms radii for the valence neutron orbits and the breathing mode constrained energies used in the fit. The breathing mode constrained energy E_0 is given by,

$$E_0 = \sqrt{\frac{m_1}{m_{-1}}} \quad (17)$$

where, fully self-consistent values for the energy-weighted (m_1) and inverse energy-weighted (m_{-1}) moments of the strength function calculated using random phase approximation (RPA) for the breathing mode (or isoscalar giant monopole resonance) can be obtained using the double commutator sum rule and the constrained HF method [13, 49], respectively. We see that all the Skyrme forces under consideration gives the similar fit to the experimental data presented in Table V.

C. Neutron skin thickness

The neutron skin thickness $r_n - r_p$ is the difference between the rms radii obtained using the density distributions for the point neutrons and point protons. It is well known [50, 51] that the accurate measurement of the neutron skin thickness would place a stringent constraint on the density dependence of the nuclear symmetry energy. In particular, it has been shown [44] that the neutron skin thickness in heavy nuclei are linearly correlated with the slope of the symmetry energy coefficient L . The value of L is poorly known due to the large uncertainty associated with the measurement of the neutron skin thickness. The measured values of the neutron skin thickness is very much probe dependent. Current data

indicate that the neutron skin thickness in the ^{208}Pb nucleus lie in the range of 0.10 – 0.28 fm [52]. The proposed experiment at the Jefferson Laboratory on parity violating electron scattering from ^{208}Pb is expected to give another independent and more accurate measurement (within 0.05 fm) of its neutron skin thickness. Recent analysis of the isospin diffusion data [44] yields $L = 88 \pm 25$ MeV which restricts the values of the neutron skin in the ^{132}Sn and ^{208}Pb nuclei to 0.29 ± 0.04 fm and 0.22 ± 0.04 fm, respectively. In Fig. 6 we present our results for neutron skin thickness obtained using GSkI, GSkII and SSk forces. The values for neutron skin thickness for the GSkI and GSkII forces are larger than those for the SSk force. It is because of the fact that the values of L for the GSkI and GSkII forces are larger than that for the SSk force (see Table IV). The values of neutron skin thickness obtained using the GSk forces for the ^{132}Sn and ^{208}Pb nuclei are in better agreement with the recent predictions 0.29 ± 0.04 and 0.22 ± 0.04 , respectively.

D. Isoscalar giant resonances

We consider now the results for the isoscalar giant monopole, dipole and quadrupole resonances obtained using the GSkI, GSkII and SSk forces. The centroid energy for the isoscalar giant monopole resonance (ISGMR) depends mainly on the value of K_∞ [53]. The centroid energy for the overtone mode of the isoscalar giant dipole resonance (ISGDR) is governed by the values of the m^* as well as K_∞ [54], whereas, the centroid energy of the isoscalar giant quadrupole resonance (ISGQR) being a surface oscillation depends merely on the value of m^* [43]. As we mentioned earlier, the correlations between the m^* and K_∞ is weaker for the GSEF which may give rise to a better agreement of the experimental data for the isoscalar giant resonances.

The excitation energy dependence of the strength function $S(E)$ for the isoscalar giant resonances is obtained using the RPA Green's function G as [55],

$$S(E) = \sum_n |\langle 0|F|n\rangle|^2 \delta(E - E_n) = \frac{1}{\pi} \text{Im} [\text{Tr}(fGf)], \quad (18)$$

where,

$$F = \sum_{i=1}^A \hat{f}(\mathbf{r}_i) \quad (19)$$

is the scattering operator with

$$\hat{f}(\mathbf{r}) = \begin{cases} r^2 Y_{00}(\hat{\mathbf{r}}) & \text{ISGMR} \\ (r^3 - \eta r) Y_{10}(\hat{\mathbf{r}}) & \text{ISGDR} \\ r^2 Y_{20}(\hat{\mathbf{r}}) & \text{ISGQR} \end{cases} \quad (20)$$

for the various isoscalar giant resonances considered. The quantity η in Eq. (20) for the case of ISGDR is taken to be equal to $\frac{5}{3}\langle r^2 \rangle$ in order to eliminate the spurious contributions arising from the center of mass motion. The RPA Green's function appearing in the Eq. (18) is obtained by discretizing the continuum [56]. The continuum is discretized by a box of 30 fm with the radial mesh size of 0.3 fm. The strength functions are smeared using a Lorentzian with the smearing parameter taken to be equal to 1.0 MeV for the purpose of plotting. We must mention that the contributions due to the spin-orbit and Coulomb interactions are ignored in evaluating the RPA Green's function, but, they are present in the HF calculations. However, neglect of spin-orbit and Coulomb interactions do not have any important bearing on our findings. It has been shown in Refs. [57, 58] that ignoring the spin-orbit and Coulomb interactions in the RPA calculations do not affect the values of the centroid energies for ^{90}Zr and ^{208}Pb nuclei as the effects of ignoring the spin-orbit interaction is counterbalanced by that for the Coulomb interaction. Further, in the present work we are mainly interested in the differences between the behaviour of the isoscalar giant resonances for the different interactions.

In Figs. 7a - 7c we have plotted the strength function for the ISGMR, ISGDR and ISGQR for the ^{208}Pb nucleus obtained using GSkI, GSkII and SSk forces. We see that for the case of ISGMR all the three forces give similar results. But, for the case of ISGDR and ISGQR the peaks at the high energy for the GSkI and GSkII forces are lowered by about 0.5 MeV in comparison to those for the SSk force. Similar trends are also observed in the ^{90}Zr nucleus (not shown). In Table VI we present our results for the centroid energy $\left(\frac{m_1}{m_0}\right)$, constrained energy $\sqrt{\frac{m_1}{m-1}}$ and scaling energy $\sqrt{\frac{m_3}{m_1}}$ for the ISGMR, ISGDR and ISGQR for the ^{90}Zr and ^{208}Pb nuclei obtained using GSkI, GSkII and SSk forces. The values of the k -th moment m_k are obtained using the strength function (Eq. 18) as,

$$m_k = \int_{E_1}^{E_2} E^k S(E) dE \quad (21)$$

where, E_1 and E_2 are the minimum and maximum values of the excitation energy over which the integration is performed. The range of the excitation energy $E_1 - E_2$ used to obtain

various energies for the isoscalar giant resonances presented in Table VI are as follows. To evaluate the ISGMR energies we have used $E_1 - E_2$ to be 0 – 40 MeV for all the cases considered. For obtaining the values of ISGDR and ISGQR energies for the ^{90}Zr (^{208}Pb) nuclei we use the integration range for the excitation energy as 18 – 40(16 – 40) and 9.5 – 40(7.5 – 40) MeV, respectively. The non-zero values for the E_1 for the case of ISGDR and ISGQR are so chosen that the low-lying peaks are excluded from the calculation of the k -th moments given by Eq. (21). The strength functions used in Eq. (21) to evaluate the moments m_k are smeared using a small value of the smearing parameter $\Gamma/2 = 0.05$ MeV. It is clear from this table that the centroid energies for the ISGDR and ISGQR obtained using GSkI and GSkII forces are in better agreement with the corresponding experimental data in comparison to those obtained using SSk force.

E. Properties of the neutron star

In this section we present our results mainly for the non-rotating neutron star obtained using the newly generated Skyrme parameter sets. In particular, we have studied the relationship between the mass and radius for the non-rotating neutron star and obtained some of the key properties for the neutron star with the “canonical” mass of $1.4M_\odot$ and for the one with maximum mass M_{max} . Bulk properties of spherically symmetric non-rotating neutron star can be obtained by integrating the Tolman-Oppenheimer-Volkoff (TOV) equation given as,

$$\frac{dP}{dr} = -\frac{G\varepsilon(r)M(r)}{r^2c^2} \left[1 + \frac{P(r)}{\varepsilon(r)} \right] \left[1 + \frac{4\pi r^3 P(r)}{M(r)c^2} \right] \left[1 - \frac{2GM(r)}{rc^2} \right]^{-1}, \quad (22)$$

and

$$\frac{dM(r)}{dr} = \frac{4\pi r^2 \varepsilon(r)}{c^2}, \quad (23)$$

where, the quantities P , ε and M are the pressure, energy density and the gravitational mass of the neutron star, respectively, which depend on the radial distance r from the center. Numerical solutions of the Eqs. (22) and (23) can be easily obtained for given initial values for the pressure $P(0)$ at the center and using $M(0) = 0$, provided, the relation between P and ε is known. For lower densities, we use Baym-Pethick-Sutherland EOS [59], matching onto the Skyrme EOS at $\rho \sim 0.5\rho_0$ and going down to $\rho = 6.0 \times 10^{-12} \text{ fm}^{-3}$. At densities larger than $0.5\rho_0$ we use the Skyrme EOS which is obtained by adding the nuclear

and leptonic contributions . The nuclear part of the energy density is obtained using Eq. (3) and following the Ref. [60]. In the leptonic sector we have considered the contributions from the electrons and muons with the corresponding energy densities ε_e and ε_μ given by,

$$\varepsilon_l = \frac{1}{\pi^2} \int_0^{k_f^l} k^2 \sqrt{k^2 + m_l^2} dk, \quad (24)$$

where, $l = e$ (electron) or μ (muon) in the above equation and k_f^l is the corresponding fermi momentum. For a given baryon density ρ , the values of the fermi momenta for the neutrons, protons, electrons and muons can be obtained by ensuring that the conditions for charge neutrality and chemical equilibrium are satisfied, i.e.,

$$\rho_p = \rho_e + \rho_\mu, \quad (25)$$

$$\mu_n = \mu_p + \mu_e, \quad (26)$$

$$\mu_e = \mu_\mu. \quad (27)$$

In Eqs. (26) and (27), μ_j denotes the chemical potential with $j = n, p, e$ or μ . Thus, the energy density depends only on the baryon density and the pressure can be obtained as,

$$P = \rho^2 \frac{d(\varepsilon/\rho)}{d\rho}. \quad (28)$$

We now consider our results for the properties of neutron stars for the GSkI and SSk forces. Results for the neutron star with the canonical mass of $1.4M_\odot$ obtained using the GSkI and GSkII forces are very much similar. Because, for both of these forces the density dependence of the symmetry energy and the pure neutron matter are quite close up to the densities $3\rho_0$. However, the GSkII force is not appropriate for the study of the neutron stars with masses larger than the canonical ones due to the undesirable feature for the symmetry energy at densities higher than $3\rho_0$ (see Fig. 1). In Fig. 8 we have plotted the variations of the proton fraction ($Y_p = \rho_p/\rho$) and electron fraction ($Y_e = \rho_e/\rho$) as a function of baryon density. The values for Y_p and Y_e or Y_μ at all the densities considered are not large enough to allow the direct Urca process. In Fig. 9 we display our results for the variations of the neutron star mass as a function of the central density ρ_c for the baryons. The relationship between the mass of the neutron star and its radius is shown in Fig. 10. In Table VII we present our results for some of the key properties associated with the neutron star with masses $1.4M_\odot$ and M_{\max} . These properties are quite similar to the ones obtained using SLy4 interaction [48]. The quantity ε_c/c^2 is the energy density at the center. The values

for baryon number (A) and binding energy (E_{bind}) for neutron star given in Table VII are obtained as follows,

$$A = \int_0^R \frac{4\pi r^2 \rho(r) dr}{\left(1 - \frac{2GM}{rc^2}\right)^{1/2}}, \quad (29)$$

and

$$E_{\text{bind}} = (Am_0 - M)c^2 \quad (30)$$

where, $m_0 = 1.66 \times 10^{-24}$ g is the mass per baryon in ^{56}Fe . We also give in Table VII the value of gravitational redshift of photons (Z_{surf}) emitted from the neutron star surface which is given as,

$$Z_{\text{surf}} = \left(1 - \frac{2GM}{Rc^2}\right)^{-1/2} - 1. \quad (31)$$

In Eqs. (29) - (31), R is the radius of neutron star with the gravitational mass M . We must point out that softening of the EOS at higher densities due to appearance of the hyperons and kaons might alter the results. In particular, results for the neutron star with the maximum mass is expected to get affected when contributions from the hyperons and kaons are also included in the EOS.

In Fig. 11 we have plotted the variation of $RP^{-1/4}$ as a function of the baryon density. Here, R is the radius (in km) of the neutron star with $1.4M_{\odot}$ and P the pressure in units of MeV/fm^3 . The solid circles denote the empirical values for the $RP^{-1/4}$ at the baryon densities $\rho/\rho_0 = 1.0, 1.5$ and 2.0 taken from Ref. [61]. In Fig. 12 we plot the ratio of neutron star binding energy to its gravitational mass as a function of the compactness parameter $\beta = \frac{GM}{Rc^2}$, R being the radius of the neutron star with gravitational mass M . The solid circles represent the empirical values obtained using the relation [62],

$$\frac{E_{\text{bind}}}{Mc^2} = \frac{0.6\beta}{1 - 0.5\beta}. \quad (32)$$

Finally, in Fig. 13 we plot the variation of moment of inertia I versus the neutron star mass. To obtain the values of I we have used the code written by Stergioulas [63]. The results presented in Fig. 13 are obtained at the Keplerian frequencies.

V. CONCLUSIONS

We have parameterized the GSEF containing multi density dependent terms of the form ρ^{ν} with $\nu = 1/3, 2/3$ and 1 in the local part of the Skyrme interaction. The experimental

data for the normal and isospin-rich nuclei are used to fit the parameters of the GSEF. Further, a realistic equation of state for the pure neutron matter upto high densities ($\sim 0.8 \text{ fm}^{-3}$) is used in the fit to ensure that the Skyrme parameters so obtained can be used to study the neutron star properties. For the appropriate comparison we generate a parameter set for the SSEF using exactly the same set of data as in the case of the GSEF. Comparing our results for the various quantities associated with the symmetric nuclear matter (at the saturation density) obtained using the parameters of GSEF and SSEF we find that the earlier one yields larger values for the isoscalar effective nucleon mass and for the quantity $L = 3\rho \frac{dJ}{d\rho}$ which is directly related to the slope of the symmetry energy coefficient J . The large value of the isoscalar effective nucleon mass is highly desirable in order to predict appropriately the location of the isoscalar giant quadrupole resonance. The value of L obtained for the GSEF is in better agreement with the ones extracted very recently [44] from the isospin diffusion data. The large value of L obtained for the parameters of the GSEF gives rise to the larger values for the neutron skin thickness corroborating recent predictions [44, 64].

The parameter sets generated in the present work for the GSEF and SSEF are used to calculate the strength function for the isoscalar giant resonances and some of the key properties for non-rotating neutron star. Calculations are performed for the strength function of the isoscalar giant monopole, dipole and quadrupole resonances for the ^{90}Zr and ^{208}Pb nuclei. We find that the results for the isoscalar giant monopole resonance are quite similar for the GSEF and SSEF parameters. However, the larger isoscalar effective nucleon mass in the case of GSEF lowers the energy of the isoscalar giant dipole and quadrupole resonances by $\sim 0.5 \text{ MeV}$ and thereby improve the agreement with experimental data. The results for the mass-radius relationship and some of the key properties for the neutron star with the “canonical” mass of $1.4M_{\odot}$ and for the one with the maximum mass are more or less same for GSEF and SSEF. We have also studied the variation of the $RP^{-1/4}$ (see Fig. 11) as a function of the baryon density which reasonably agrees with the empirical values [61]. The comparison with the empirical values were also done for the variation of the ratio of the binding energy of the neutron star to its gravitational mass as a function of the compactness parameter.

Acknowledgments

We would like to thank J. N. De and S. K. Samaddar for their helpful comments and for reading the manuscript. We also acknowledge the discussions with D. Bandyopadhyay.

-
- [1] J. S. Bell and T. H. R. Skyrme, *Phil. Mag.* **1**, 1055 (1956).
- [2] D. Vautherin and D. M. Brink, *Phys. Rev. C* **5**, 626 (1972).
- [3] L. Zamick, *Phys. Lett.* **B45**, 313 (1973).
- [4] N. V. Giai and H. Sagawa, *Phys. Lett.* **106B**, 379 (1981).
- [5] J. Bartel, P. Quentin, M. Brack, C. Guet, and H. B. Hakansson, *Nucl. Phys.* **A386**, 79 (1982).
- [6] F. Tondeur, M. Brack, M. Farine, and J. M. Pearson, *Nucl. Phys.* **A420**, 297 (1984).
- [7] J. M. Pearson, Y. Aboussir, A. K. Dutta, R. C. Nayak, and M. F. Tondeur, *Nucl. Phys.* **A528**, 1 (1990).
- [8] P. G. Reinhard and H. Flocard, *Nucl. Phys.* **A584**, 467 (1995).
- [9] E. Chabanat, P. Bonche, P. Haensel, J. Meyer, and R. Schaeffer, *Nucl. Phys.* **A635**, 231 (1998).
- [10] B. A. Brown, *Phys. Rev. C* **58**, 220 (1998).
- [11] M. Bender, P. H. Heenen, and P.-G. Reinhard, *Rev. Mod. Phys.* **75**, 121 (2003).
- [12] S. Goriely, M. Samyn, P.-H. Heenen, J. M. Pearson, and M. Onsi, *Nucl. Phys.* **A750**, 425 (2005).
- [13] B. K. Agrawal, S. Shlomo, and V. K. Au, *Phys. Rev. C* **72**, 014310 (2005).
- [14] T. Duguet and P. Bonche, *Physical Review C* **67**, 054308 (2003).
- [15] B. Cochet, K. Bennaceur, P. Bonche, T. Duguet, and J. Meyer, *Nucl. Phys.* **A731**, 34 (2004).
- [16] B. Cochet, K. Bennaceur, J. Meyer, P. Bonche, and T. Duguet, *Int. J. Mod. Phys. E* **13**, 187 (2004).
- [17] A. Bhattacharyya and R. J. Furnstahl, *Nucl. Phys.* **A747**, 268 (2005).
- [18] N. Kaiser, S. Fritsch, and W. Weise, *Nucl. Phys.* **A697**, 255 (2002).
- [19] K.-F. Liu, H. Luo, Z. Ma, and Q. Shen, *Nucl. Phys.* **A534**, 1 (1991).
- [20] K.-F. Liu, H. Luo, Z. Ma, Q. Shen, and S. A. Mozkowski, *Nucl. Phys.* **A534**, 25 (1991).
- [21] K.-F. Liu, Z. yu Ma, M. Feng, and Q. Shen, *Nucl. Phys.* **A534**, 48 (1991).
- [22] M. Farine, J. M. Pearson, and F. Tondeur, *Nucl. Phys.* **A615**, 135 (1997).
- [23] M. Beiner, H. Flocard, N. V. Giai, and P. Quentin, *Nucl. Phys.* **A238**, 29 (1975).
- [24] M. Bender, J. Dobaczewski, J. Engel, and W. Nazarewicz, *Phys. Rev. C* **65**, 054322 (2002).
- [25] S. Shlomo, *Rep. Prog. Phys.* **41**, 957 (1978).

- [26] W. Bertozzi, J. Friar, J. Heisenberg, and J. W. Negele, Phys. Lett. **B41**, 408 (1972).
- [27] S. Shlomo and W. G. Love, Phys. Scr. **26**, 280 (1982).
- [28] S. Goriely, M. Samyn, P.-H. Heenen, J. M. Pearson, and F. Tondeur, Phys. Rev. C **66**, 024326 (2002).
- [29] S. Kirkpatrik, J. Stat. Phys. **34**, 975 (1984).
- [30] L. Ingber, Mathl. Comput. Modelling **12**, 967 (1989).
- [31] B. Cohen, Master's thesis, Tel-Aviv University (1994).
- [32] T. Bürvenich, D. G. Madland, J. A. Maruhn, and P.-G. Reinhard, Phys. Rev. C **65**, 044308 (2002).
- [33] T. J. Bürvenich, D. G. Madland, and P.-G. Reinhard, Nucl. Phys. **A744**, 92 (2004).
- [34] G. Audi, A. H. Wapstra, and C. Thibault, Nucl. Phys. **A729**, 337 (2003).
- [35] E. W. Otten, *in Treatise on Heavy-Ion Science*, vol. 8 (ed. D. A. Bromley, Plenum, New York, 1989).
- [36] H. D. Vries, C. W. D. Jager, and C. D. Vries, At. Data Nucl. Data Tables **36**, 495 (1987).
- [37] N. Kalantar-Nayestanaki, , H. Baghaei, W. Bertozzi, S. Dixit, J. M. Finn, C. E. Hyde-Wright, S. Kowalski, R. W. Lourie, C. P. Sargent, et al., Phys. Rev. Lett. **60**, 1707 (1988).
- [38] S. Platchkov, A. Amroun, P. Bricault, J. M. Cavedon, P. K. A. de Witt Huberts, P. Dreux, B. Frois, C. D. Goodman, D. Goutte, J. Martino, et al., Phys. Rev. Lett. **61**, 1465 (1988).
- [39] A. Bohr and B. R. Mottelson, *Nuclear Structure*, vol. Vol. I (Benjamin, New York, 1969).
- [40] B. A. Brown, private communication (2005).
- [41] D. H. Youngblood, H. L. Clark, and Y. W. Lui, Phys. Rev. Lett. **82**, 691 (1999).
- [42] R. Wiringa, V. Fiks, and A. Fabrocini, Phys. Rev. C **38**, 1010 (1988).
- [43] P. G. Reinhard, Nucl. Phys. **A649**, 305c (1999).
- [44] L.-W. Chen, C. M. Ko, and B.-A. Li, Nucl-th **0509009** (2005).
- [45] M. Kutschera, Phys. Lett. **B340**, 1 (1994).
- [46] M. Kutschera and J. Niemiec, Phys. Rev. C **62**, 025802 (2000).
- [47] J. M. Lattimer, C. J. Pethick, M. Prakash, and P. Haensel, Phys. Rev. Lett. **66**, 2701 (1991).
- [48] J. R. Stone, J. C. Miller, R. Koncewicz, P. D. Stevenson, and M. R. Strayer, Phys. Rev. C **68**, 034324 (2003).
- [49] O. Bohigas, A. M. Lane, and J. Martorell, Phys. Rep. **51**, 267 (1979).
- [50] B. A. Brown, Phys. Rev. Lett. **85**, 5296 (2000).

- [51] C. J. Horowitz and J. Piekarewicz, *Phys. Rev. Lett.* **86**, 5647 (2001).
- [52] A. Krasznahorkay, H. Akimune, A. van den Berg, N. Blasi, S. Brandenburg, M. Csatlos, M. Fujiwara, J. Gulyas, M. Harakeh, and M. H. et al., *Nucl. Phys.* **A731**, 224 (2004).
- [53] J. P. Blaizot, J. F. Berger, J. Decharge, and M. Girod, *Nucl. Phys.* **A591**, 435 (1995).
- [54] V. Kolomietz and S. Shlomo, *Phys. Rev. C* **61**, 064302 (2000).
- [55] S. Shlomo and G. F. Bertsch, *Nucl. Phys.* **A243**, 507 (1975).
- [56] S. Shlomo and A. I. Sanzhur, *Phys. Rev. C* **65**, 044310 (2002).
- [57] B. K. Agrawal, S. Shlomo, and V. K. Au, *Phys. Rev. C* **70**, 014308 (2004).
- [58] T. Sil, S. Shlomo, B. K. Agrawal, and P. G. Reinhard, *Phys. Rev. C* (Submitted).
- [59] B. Gordon, P. Christopher, and S. Peter, *Astrophysical Journal* **170**, 299 (1971).
- [60] E. Chabanat, P. Bonche, P. Haensel, J. Meyer, and R. Schaeffer, *Nucl. Phys.* **A627**, 710 (1997).
- [61] J. M. Lattimer and B. F. Schutz, *Astrophys. J.* **629**, 979 (2005).
- [62] J. M. Lattimer and M. Prakash, *Astrophys. J.* **550**, 426 (2001).
- [63] N. Stergioulas and J. L. Friedman, *Astrophys. J.* **444**, 306 (1995).
- [64] B. G. Todd-Rutel and J. Piekarewicz, *Phys. Rev. Lett* **95**, 122501 (2005).
- [65] D. H. Youngblood, Y.-W. Lui, B. John, Y. Tokimoto, H. L. Clark, and X. Chen, *Phys. Rev. C* **69**, 054312 (2004).
- [66] D. H. Youngblood, Y.-W. Lui, H. L. Clark, B. John, Y. Tokimoto, and X. Chen, *Phys. Rev. C* **69**, 034315 (2004).

FIG. 1: The density dependence of the symmetry energy coefficient $J(\rho)$ for the GSkI, GSkII and SSk forces.

FIG. 2: The EOS of nuclear matter for the proton fractions $Y_p = 0, 0.25, 0.4$ and 0.5 for the GSkI, GSkII and SSk forces. The solid squares represent the EOS for pure neutron matter (i.e., $Y_p = 0$) obtained for the UV14+UVII model [42].

FIG. 3: Comparison of the results for the relative errors, $\Delta B = (B^{expt} - B^{th})/B^{expt}$, in the values of binding energies for the nuclei considered in the fit to obtain the GSkI, GSkII and SSk forces. A=48 represents the result for ^{48}Ca nucleus. The result for ^{48}Ni nucleus is discussed in the text. The rms error for the total binding energy are 1.18, 1.72 and 1.28 MeV for the GSkI, GSkII and SSk forces, respectively.

FIG. 4: Comparison of the results for the relative errors, $\Delta r_{ch} = (r_{ch}^{expt} - r_{ch}^{th})/r_{ch}^{expt}$, in the values for the charge rms radii for nuclei considered in the fit to obtain the GSkI, GSkII and SSk forces. The rms error for the charge rms radii are 0.023, 0.026 and 0.021 fm for the GSkI, GSkII and SSk forces, respectively.

FIG. 5: The single particle energies for ^{208}Pb obtained using GSkI, GSkII and SSk forces are compared with the experimental data for (a) neutrons and (b) protons. The rms error in the single particle energies are 1.44, 1.13 and 1.67 MeV for the GSkI, GSkII and SSk forces, respectively.

FIG. 6: Comparison of neutron skin thickness, $r_n - r_p$ for the GSkI, GSkII and SSk forces. The values for neutron skin thickness for ^{132}Sn and ^{208}Pb nuclei represented by filled circles are the recent prediction based on isospin diffusin data [44]. A=48 represents the result for ^{48}Ca nucleus. The result for ^{48}Ni is discussed in the text.

FIG. 7: Variations of the strength function with excitation energy for the (a)isoscalar giant monopole resonance, (b)isoscalar giant dipole resonance and (c)isoscalar giant quadrupole resonance. The results are obtained using GSkI, GSkII and SSk forces for the ^{208}Pb nucleus.

FIG. 8: Variations of the proton and electron fractions with the baryon density for the GSkI and SSk forces.

FIG. 9: The neutron star mass as a function of the central baryon density ρ_c for the GSkI and SSk forces.

FIG. 10: Relation between the neutron star mass and its radius R for the GSkI and SSk forces.

FIG. 11: Variation of $RP^{-1/4}$ as a function of the baryon density ρ . Here, R is the radius (in km) for the neutron star of $1.4M_\odot$ and P is the pressure in units of MeV/fm^3 . The solid circles represent the empirical values taken from Ref. [61].

FIG. 12: Ratio of the neutron star binding energy E_{bind} to its corresponding gravitational mass M as a function of the compactness parameter $\beta = \frac{GM}{Rc^2}$. The solid circles represent the empirical values calculated using Eq. (32).

FIG. 13: Moment of inertia I as a function of the neutron star mass. The values of I are obtained at the Keplerian frequencies.

TABLE I: The lower (\mathbf{v}_0) and upper (\mathbf{v}_1) limits, maximum displacement (\mathbf{d}) and initial values (\mathbf{v}_{in}) for the Skyrme parameters used to minimize the χ^2 value within the SAM.

	\mathbf{v}_0	\mathbf{v}_1	\mathbf{d}	\mathbf{v}_{in}
$t_0(\text{MeV}\cdot\text{fm}^3)$	-3000.0	-1500.0	50.0	-1603.0
$t_1(\text{MeV}\cdot\text{fm}^5)$	-500.0	500.0	20.0	515.9
$t_2(\text{MeV}\cdot\text{fm}^5)$	-500.0	500.0	20.0	84.5
$t_{31}(\text{MeV}\cdot\text{fm}^{3(\alpha_1+1)})$	1000.0	3000.0	50.0	1333.3
$t_{32}(\text{MeV}\cdot\text{fm}^{3(\alpha_2+1)})$	-1000	0.0	50.0	0.0
$t_{33}(\text{MeV}\cdot\text{fm}^{3(\alpha_3+1)})$	-500.0	500.0	20.0	0.0
x_0	-4.0	4.0	0.1	-0.02
x_1	-4.0	4.0	0.1	-0.5
x_2	-4.0	4.0	0.1	-1.713
x_{31}	-4.0	4.0	0.1	0.1381
x_{32}	-4.0	4.0	0.1	0.0
x_{33}	-4.0	4.0	0.1	0.0
α_1	$\frac{1}{3}$	$\frac{1}{3}$	0	$\frac{1}{3}$
α_2	$\frac{2}{3}$	$\frac{2}{3}$	0	$\frac{2}{3}$
α_3	1	1	0	1
$W_0(\text{MeV}\cdot\text{fm}^5)$	100.0	200.0	5.0	125.0
$V_w(\text{MeV})$	-3.0	0.0	0.2	-2.05
$V_{w'}(\text{MeV})$	0.0	2.0	0.1	0.697
λ	400.0	600.0	10.0	485.0
A_0	10.0	50.0	1.0	28.0

TABLE II: Selected experimental data for the binding energies B , charge rms radii r_{ch} , rms radii of valence neutron orbits r_v , single-particle energies (S-P), breathing mode constrained energies E_0 and EOS for the pure neutron matter used in the fit to determine the parameters of the Skyrme interaction.

Properties	Nuclei	Ref.
B	$^{16,24}\text{O}$, $^{40,48}\text{Ca}$, $^{48,56,68,78}\text{Ni}$, ^{88}Sr , ^{90}Zr , $^{100,132}\text{Sn}$, ^{208}Pb	[34]
r_{ch}	^{16}O , $^{40,48}\text{Ca}$, ^{56}Ni , ^{88}Sr , ^{90}Zr , ^{208}Pb	[35, 36]
$r_v(\nu 1d_{5/2})$	^{17}O	[37]
$r_v(\nu 1f_{7/2})$	^{41}Ca	[38]
S-P energies	^{208}Pb	[39, 40]
E_0	^{90}Zr and ^{208}Pb	[41]
EOS	pure neutron matter	[42]

TABLE III: The values of the Skyrme parameters for GSkI, GSkII and SSk interactions obtained by minimizing the χ^2 .

	GSkI	GSkII	SSk
$t_0(\text{MeV}\cdot\text{fm}^3)$	-1855.45	-1855.99	-2523.52
$t_1(\text{MeV}\cdot\text{fm}^5)$	397.23	393.08	435.00
$t_2(\text{MeV}\cdot\text{fm}^5)$	264.63	266.08	-382.04
$t_{31}(\text{MeV}\cdot\text{fm}^{3(\alpha_1+1)})$	2309.67	2307.15	2372.49
$t_{32}(\text{MeV}\cdot\text{fm}^{3(\alpha_2+1)})$	-449.01	-448.28	--
$t_{33}(\text{MeV}\cdot\text{fm}^{3(\alpha_3+1)})$	-53.31	--	--
x_0	0.1180	0.0909	0.6835
x_1	-1.7586	-0.7203	-0.4519
x_2	-1.8068	-1.8369	-0.9214
x_{31}	0.1261	-0.1005	1.0508
x_{32}	-1.1881	-0.3529	--
x_{33}	-0.4594	--	--
α_1	$\frac{1}{3}$	$\frac{1}{3}$	0.1682
α_2	$\frac{2}{3}$	$\frac{2}{3}$	--
α_3	1	--	--
$W_0(\text{MeV}\cdot\text{fm}^5)$	169.57	152.28	131.98
$V_w(\text{MeV})$	-2.9944	-2.6683	-1.2124
$V_{w'}(\text{MeV})$	0.7059	0.6191	0.3077
λ	538.23	442.56	461.43
A_0	49.91	47.24	19.33

TABLE IV: Nuclear matter properties for the GSkI, GSkII and SSk interactions at the minimum value of χ^2 . The quantities given below are: B/A the binding energy per nucleon, K_∞ the nuclear matter incompressibility coefficient, J the symmetry energy, $L = 3\rho\frac{dJ}{d\rho}$ related to the slope of the symmetry energy, m^*/m is the ratio of the isoscalar effective nucleon mass to the bare nucleon mass and ρ_s the saturation density. Values for these quantities are obtained at the saturation density.

Parameter	GSkI	GSkII	SSk
B/A (MeV)	16.02	16.13	16.15
K_∞ (MeV)	230.20	233.60	229.17
J (MeV)	32.03	34.15	33.49
L (MeV)	63.46	66.82	52.75
m^*/m	0.78	0.79	0.72
ρ_s	0.159	0.159	0.161

TABLE V: The rms radii of the valence neutron orbits r_v (fm) and the breathing mode constrained energies (MeV). The experimental values (and the theoretical error σ) used in the fit to determine the Skyrme parameters are taken as follows: the values of r_v were taken from Ref. [37, 38] ($\sigma = 0.06$ fm) and values of the breathing mode constrained energies were taken from [41] ($\sigma = 0.5$ MeV for the ^{90}Zr nucleus and $\sigma = 0.3$ MeV for ^{208}Pb nucleus). The superscript ‘ a ’ denotes that the corresponding data were not included in the fit.

		Exp.	GSkI	GSkII	SSk
r_v	$(\nu 1d_{5/2})$	3.36	3.35	3.37	3.34
	$(\nu 1f_{7/2})$	3.99	4.01	4.02	4.05
E_0	^{90}Zr	17.81	18.12	18.17	18.03
	$^{116}\text{Sn}^a$	15.90	16.52	16.59	16.43
	$^{144}\text{Sm}^a$	15.25	15.62	15.67	15.52
	^{208}Pb	14.18	13.69	13.70	13.66

TABLE VI: Values of the centroid energy $\left(\frac{m_1}{m_0}\right)$, constrained energy $\sqrt{\frac{m_1}{m_{-1}}}$ and scaling energy $\sqrt{\frac{m_3}{m_1}}$ obtained using strength function calculated within the RPA frame work. The experimental data given here are taken from Refs. [41, 65, 66].

Nuclei	Interaction	$\frac{m_1}{m_0}$	$\sqrt{\frac{m_1}{m_{-1}}}$	$\sqrt{\frac{m_3}{m_1}}$	Γ
<i>ISGMR</i>					
^{90}Zr	GSkI	18.48	18.25	19.14	2.70
	GSkII	18.60	18.36	19.25	2.72
	SSk	18.43	18.20	19.05	2.63
	Exp.	17.89	17.81		
^{208}Pb	GSkI	13.79	13.55	14.46	2.33
	GSkII	13.79	13.55	14.46	2.33
	SSk	13.87	13.64	14.53	2.31
	Exp.	14.17	14.18		
<i>ISGDR</i>					
^{90}Zr	GSkI	28.56	28.11	29.74	4.82
	GSkII	28.48	28.03	29.69	4.87
	SSk	28.83	28.38	30.04	4.90
	Exp.	26.7			
^{208}Pb	GSkI	24.14	23.87	24.95	3.60
	GSkII	23.78	23.50	24.65	3.69
	SSk	24.61	24.32	25.46	3.73
	Exp.	22.20			
<i>ISGQR</i>					
^{90}Zr	GSkI	14.65	14.50	15.52	2.65
	GSkII	14.42	14.29	15.22	2.50
	SSk	15.10	14.98	15.86	2.50
	Exp.	14.30			
^{208}Pb	GSkI	11.34	11.23	12.10	2.10
	GSkII	11.07	10.97	11.82	2.05
	SSk	11.92	11.80	12.71	2.23
	Exp.	10.89			

TABLE VII: Some of the key properties of the neutron star with $1.4M_{\odot}$ and the maximum mass M_{\max} calculated using the GSkI and SSk forces.

	$1.4M_{\odot}$		M_{\max}	
	<i>GSkI</i>	<i>SSk</i>	<i>GSkI</i>	<i>SSk</i>
ρ_c (fm^{-3})	0.53	0.55	1.21	1.22
ε_c/c^2 (10^{14} g cm^{-3})	9.68	10.03	27.97	28.54
$M(M_{\odot})$	1.40	1.40	1.95	2.00
R (km)	11.97	11.62	10.05	9.87
A (10^{57})	1.81	1.82	2.68	2.77
E_{bind} (10^{53} erg)	2.03	2.09	5.09	5.59
z_{surf}	0.24	0.25	0.53	0.58

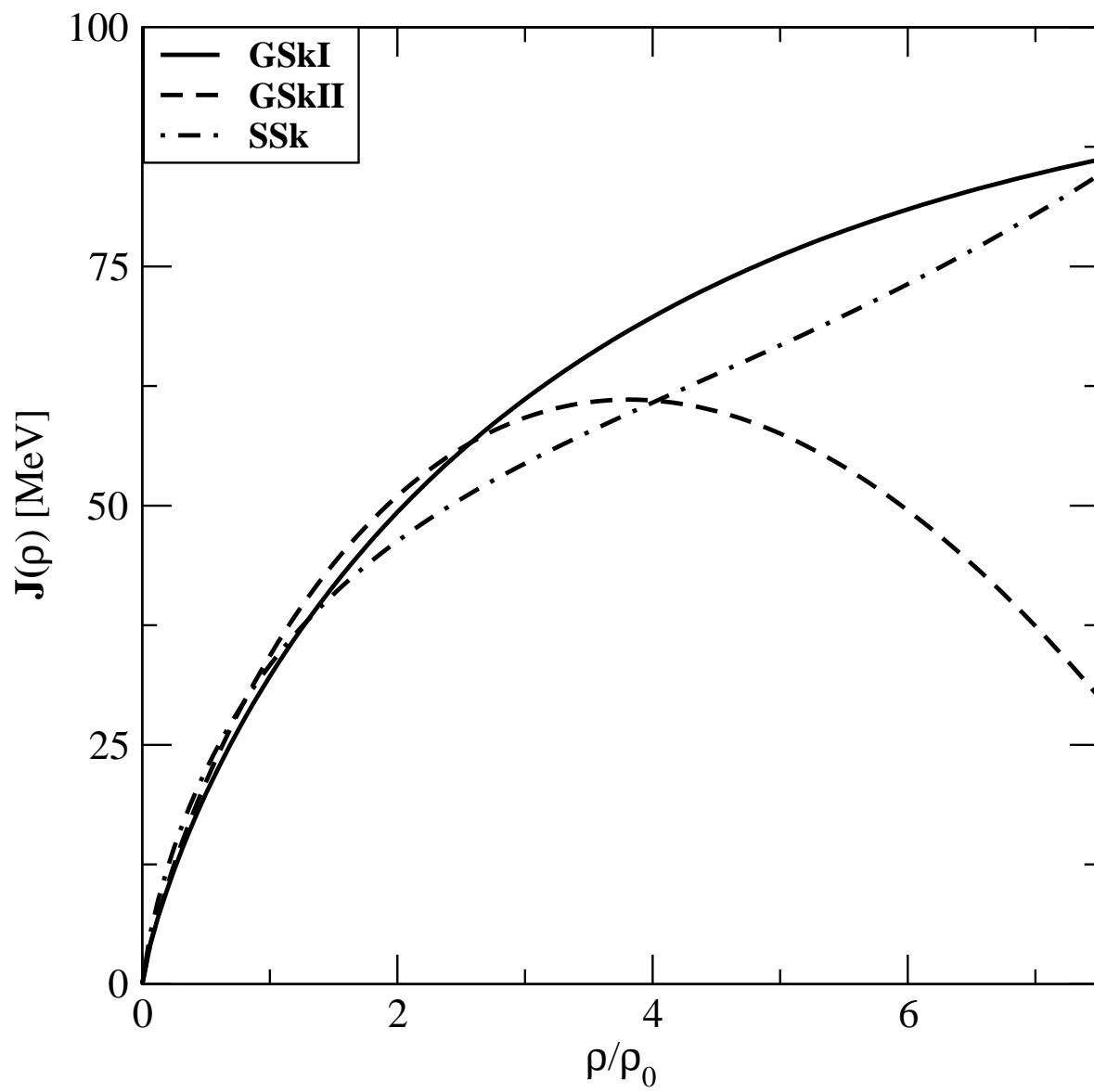


Fig. 1

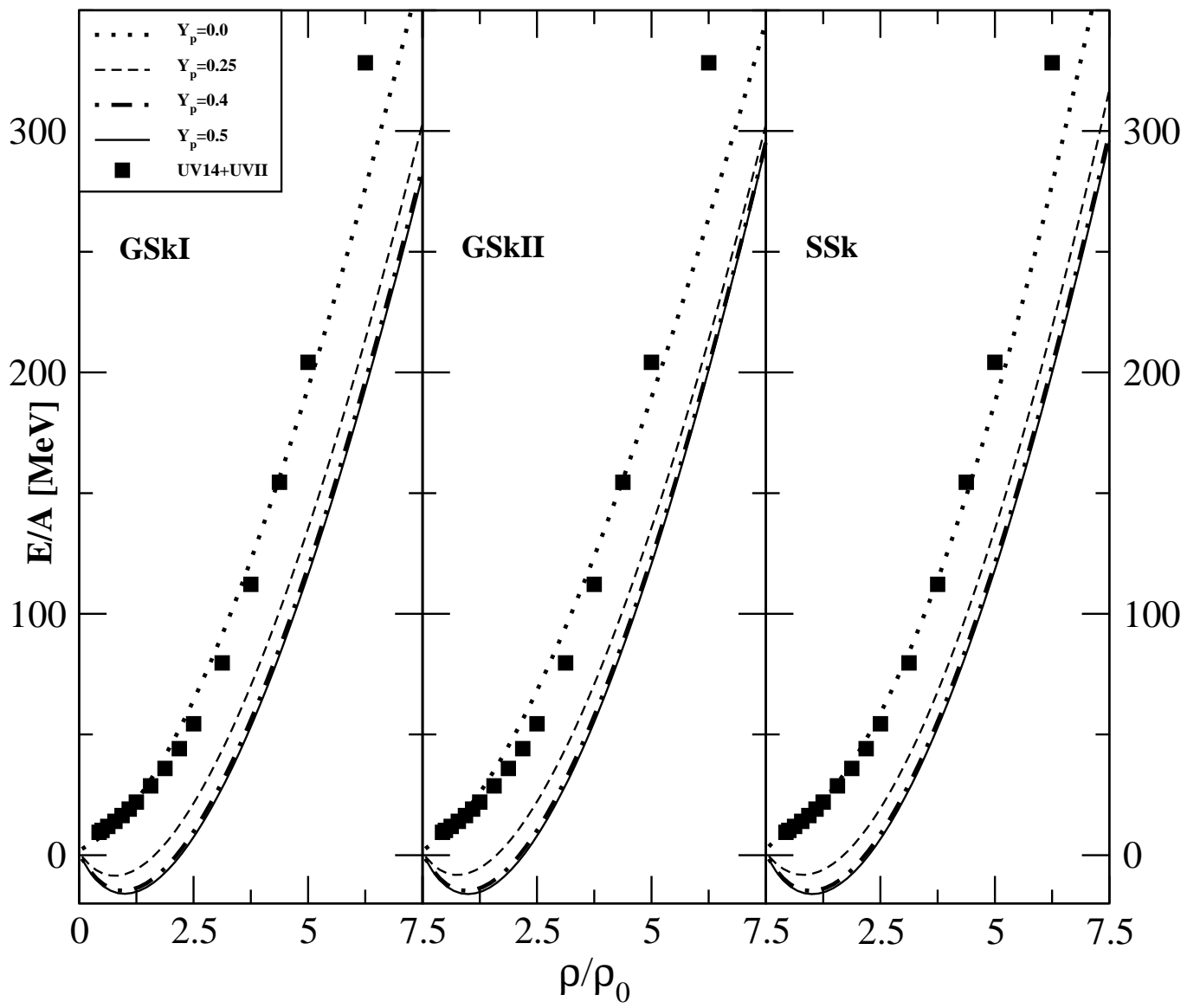


Fig. 2

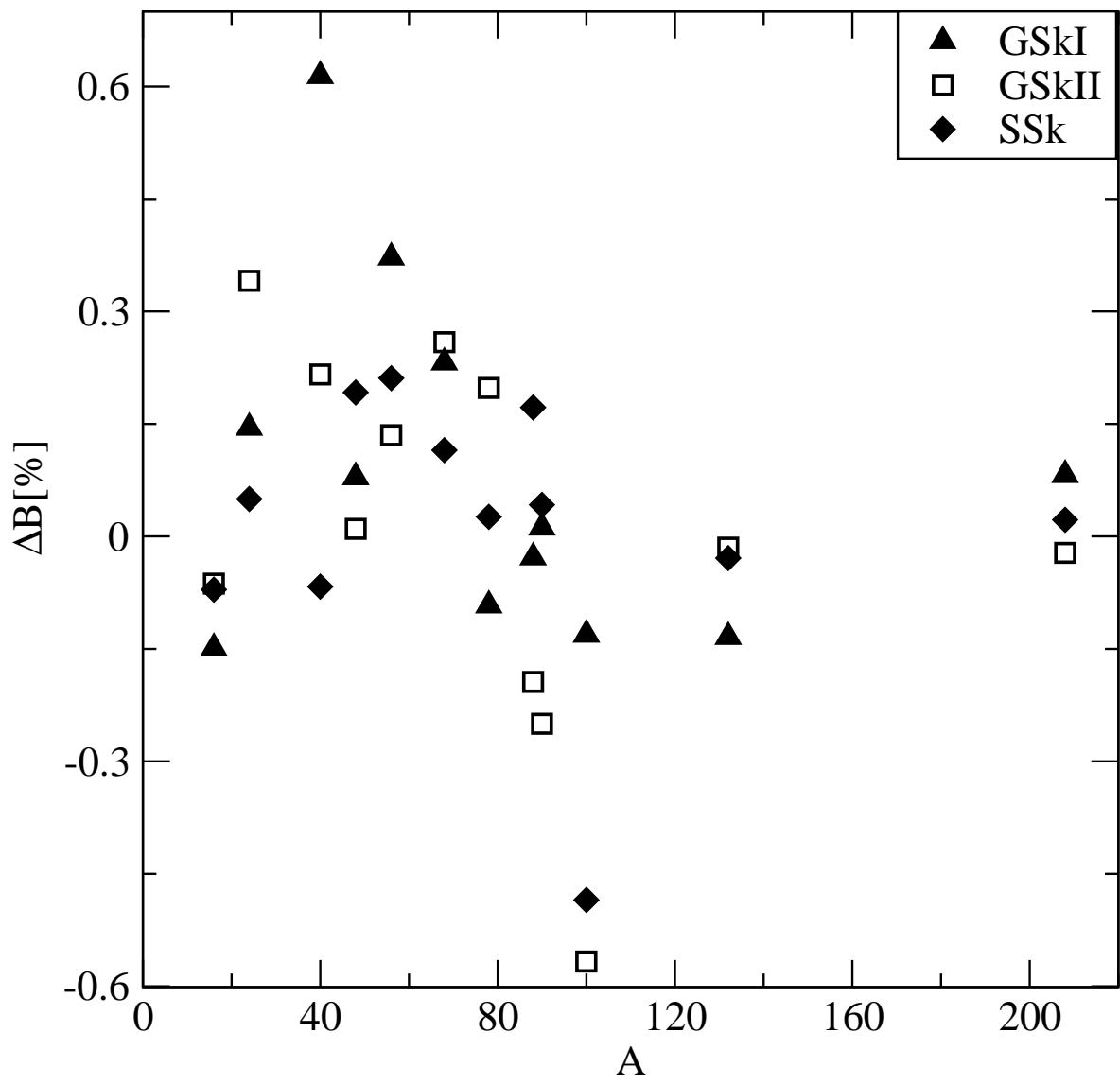


Fig.3

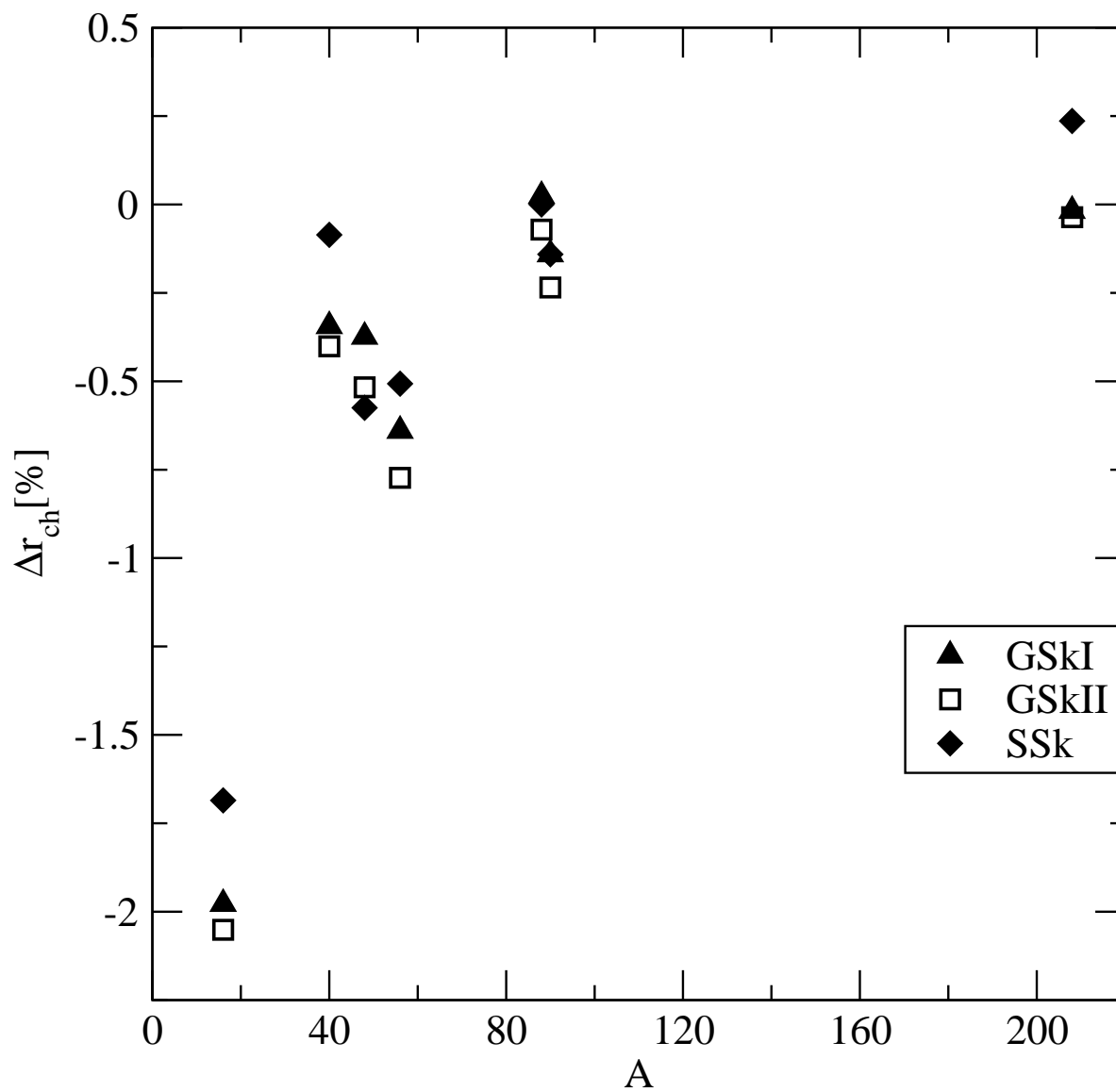


Fig.4

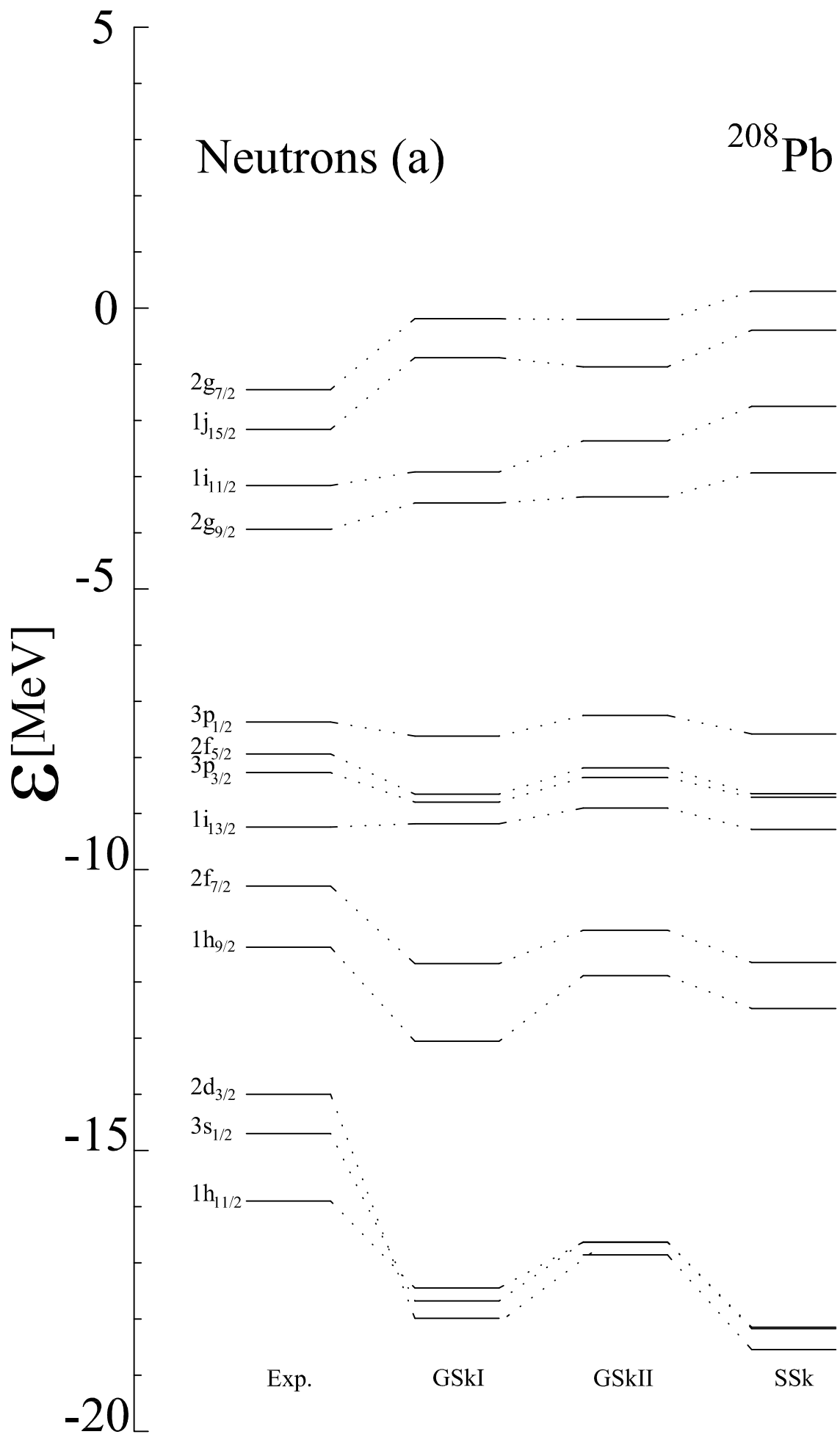


Fig. 5a

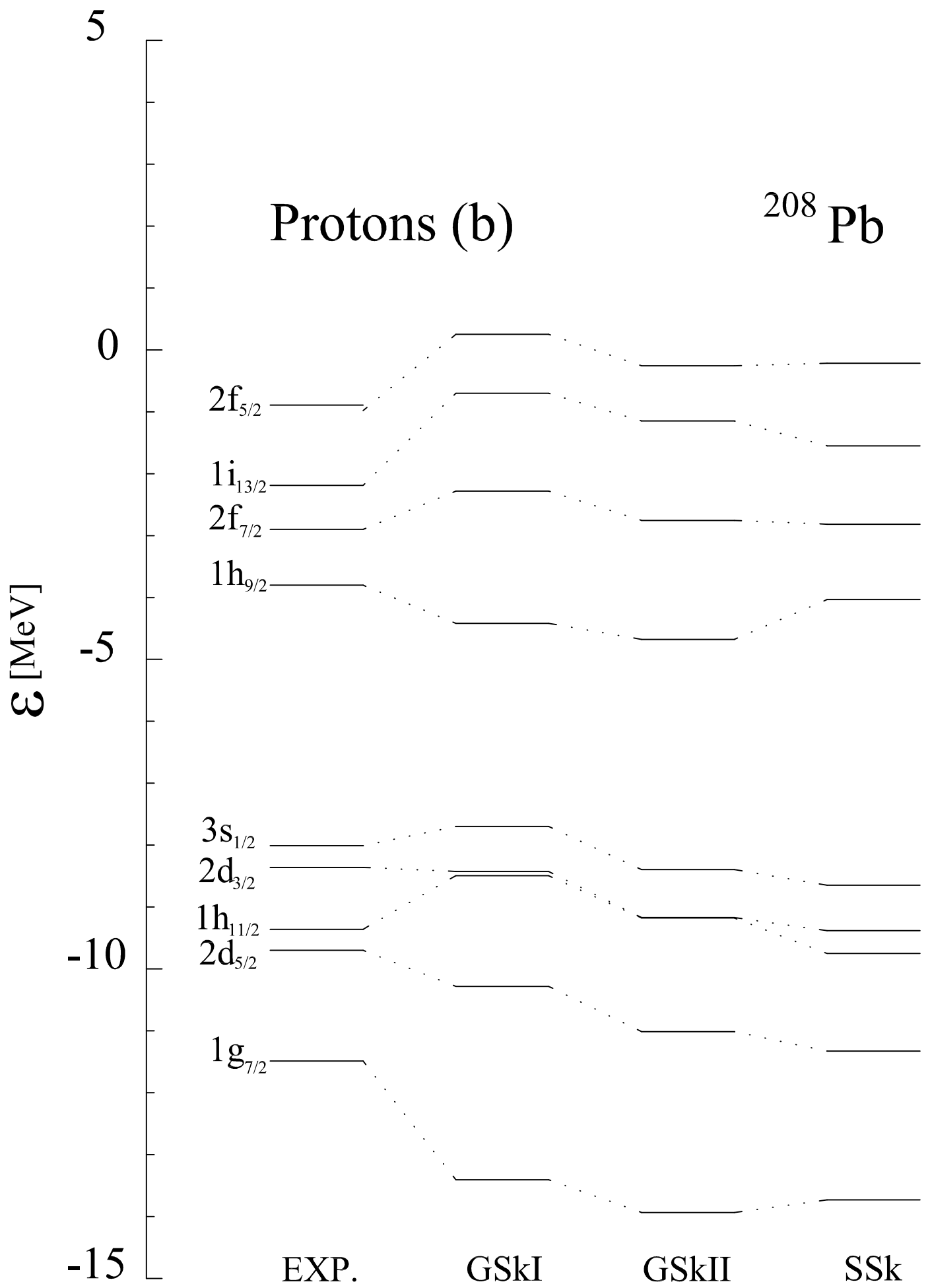


Fig. 5b

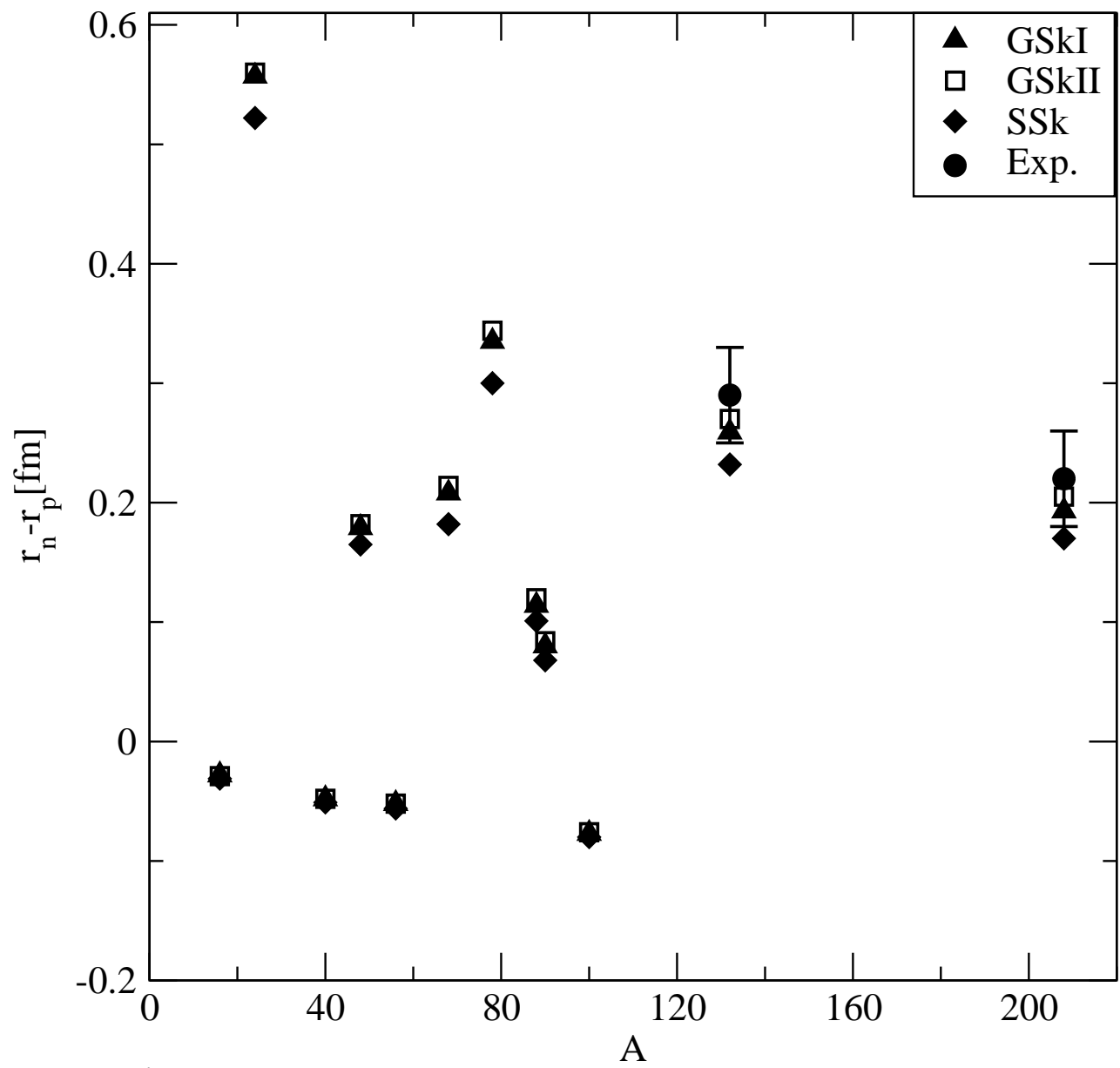


Fig.6

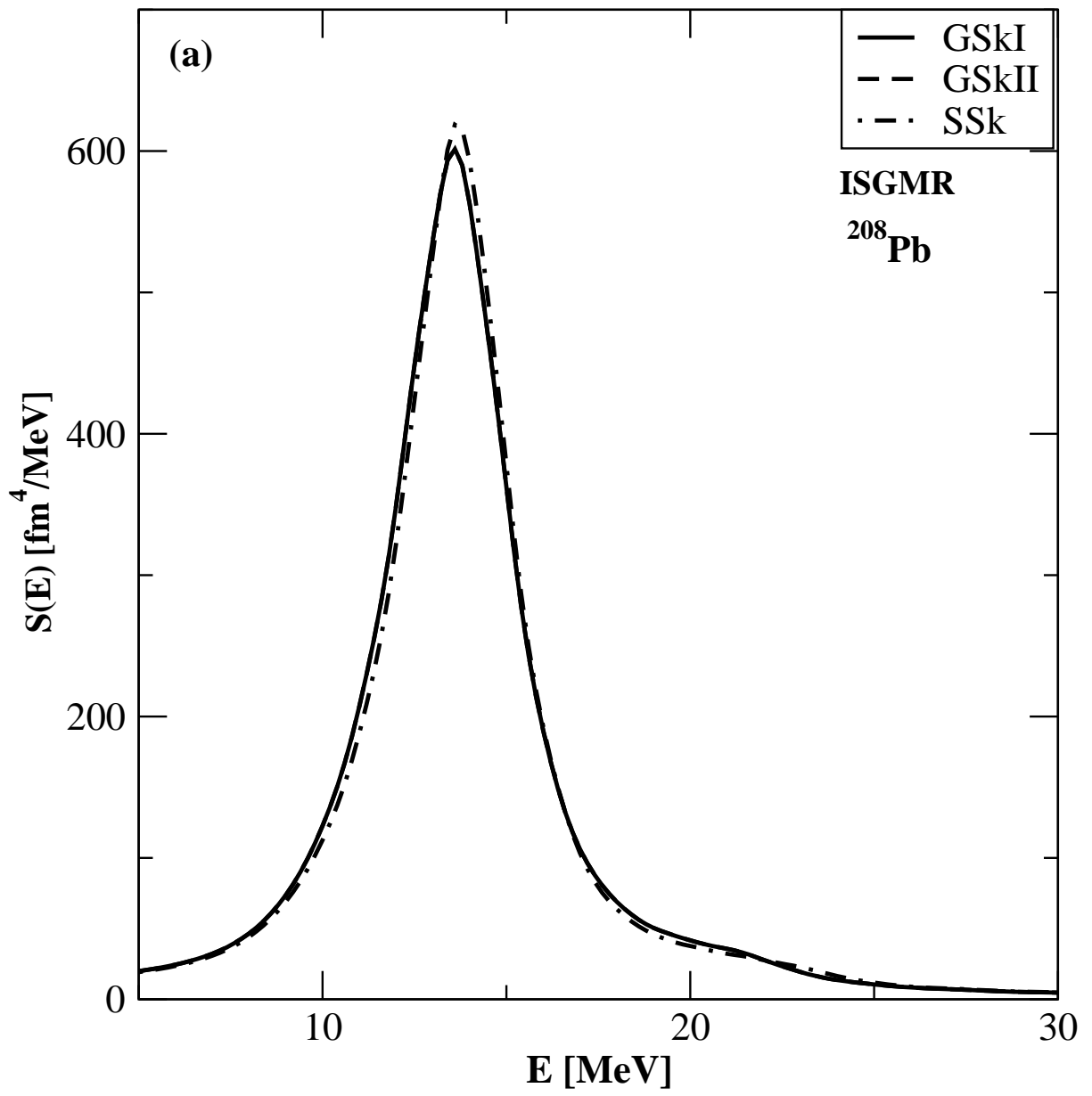


Fig. 7a

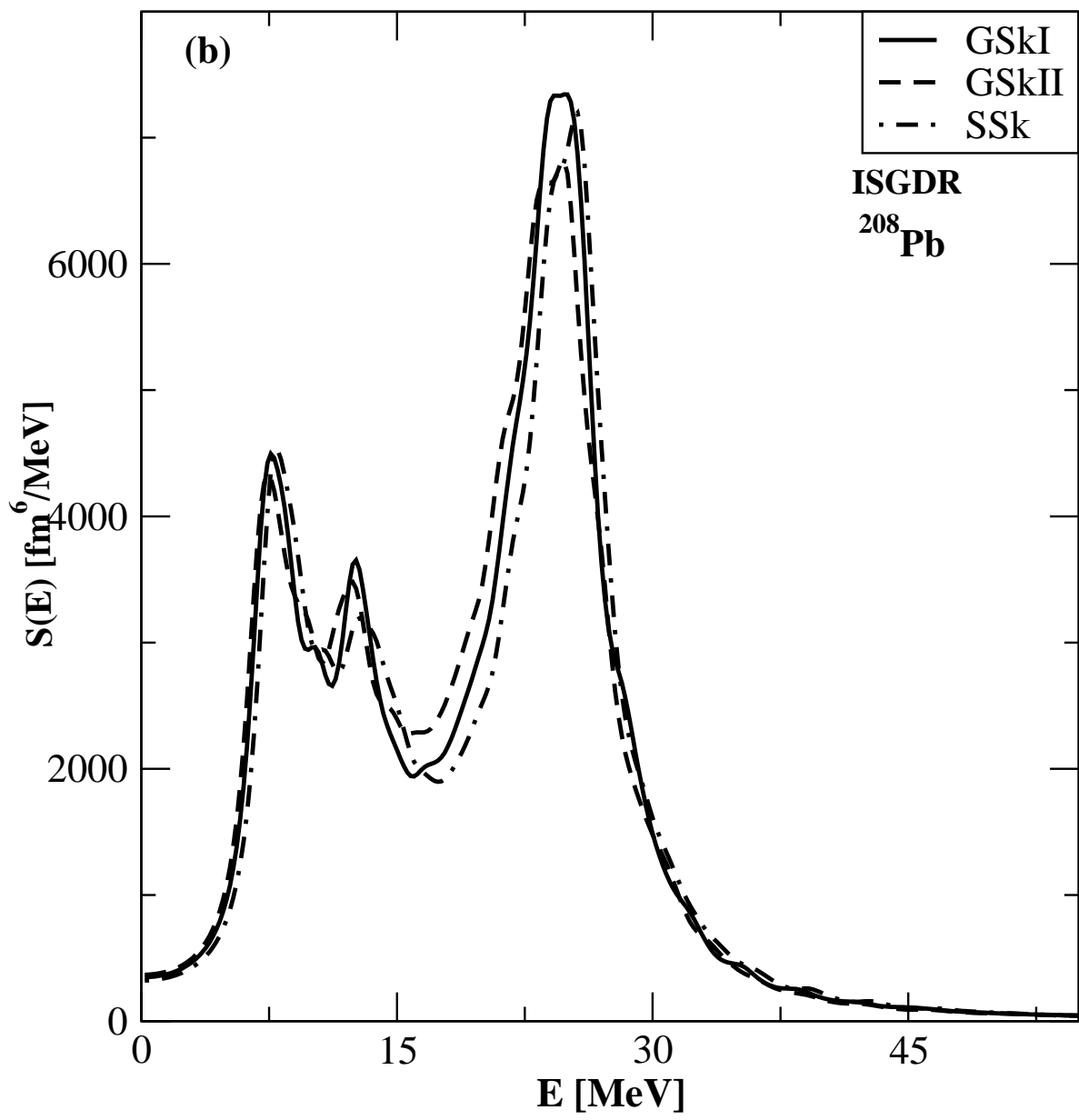


Fig. 7b

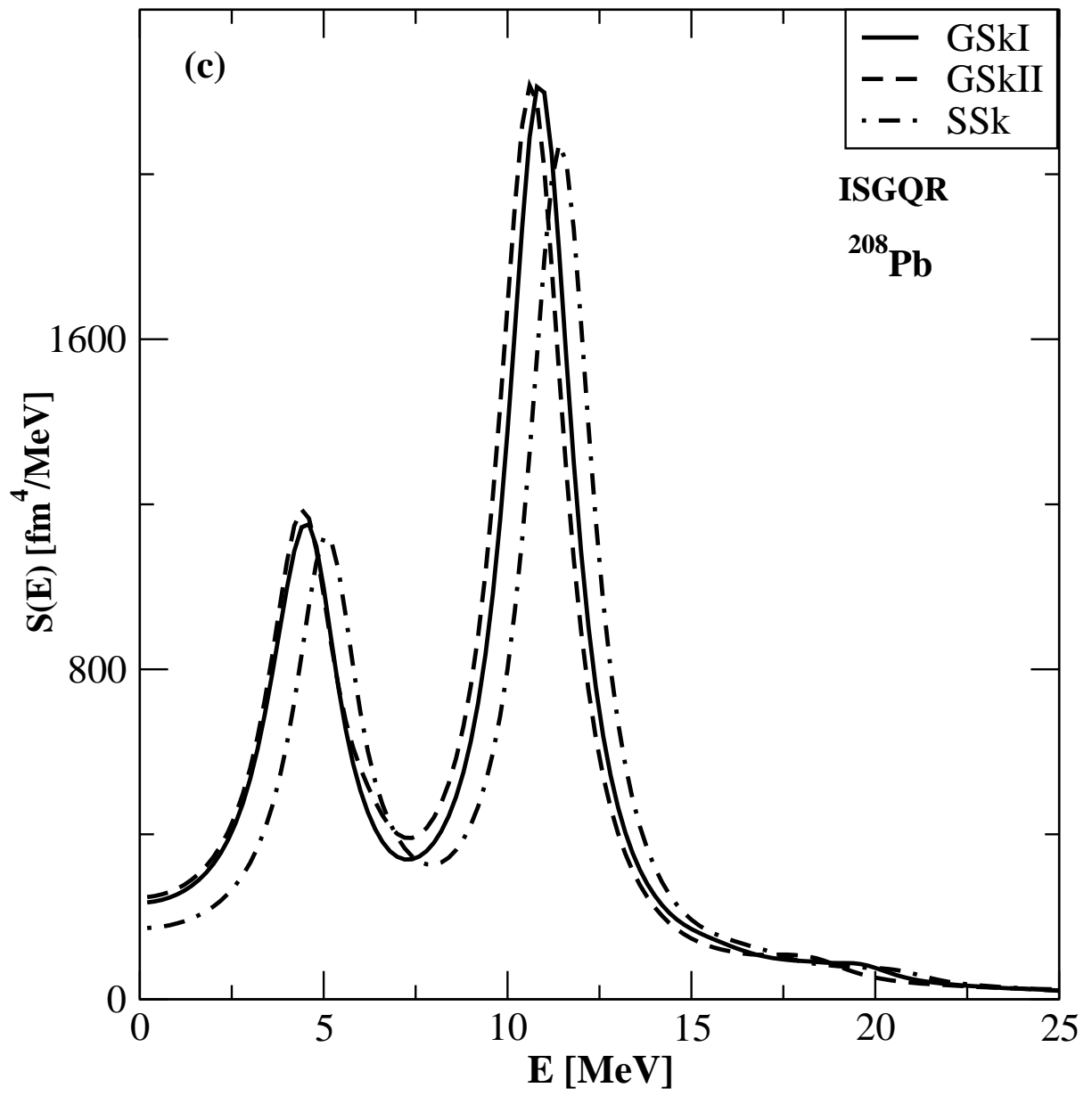


Fig. 7c

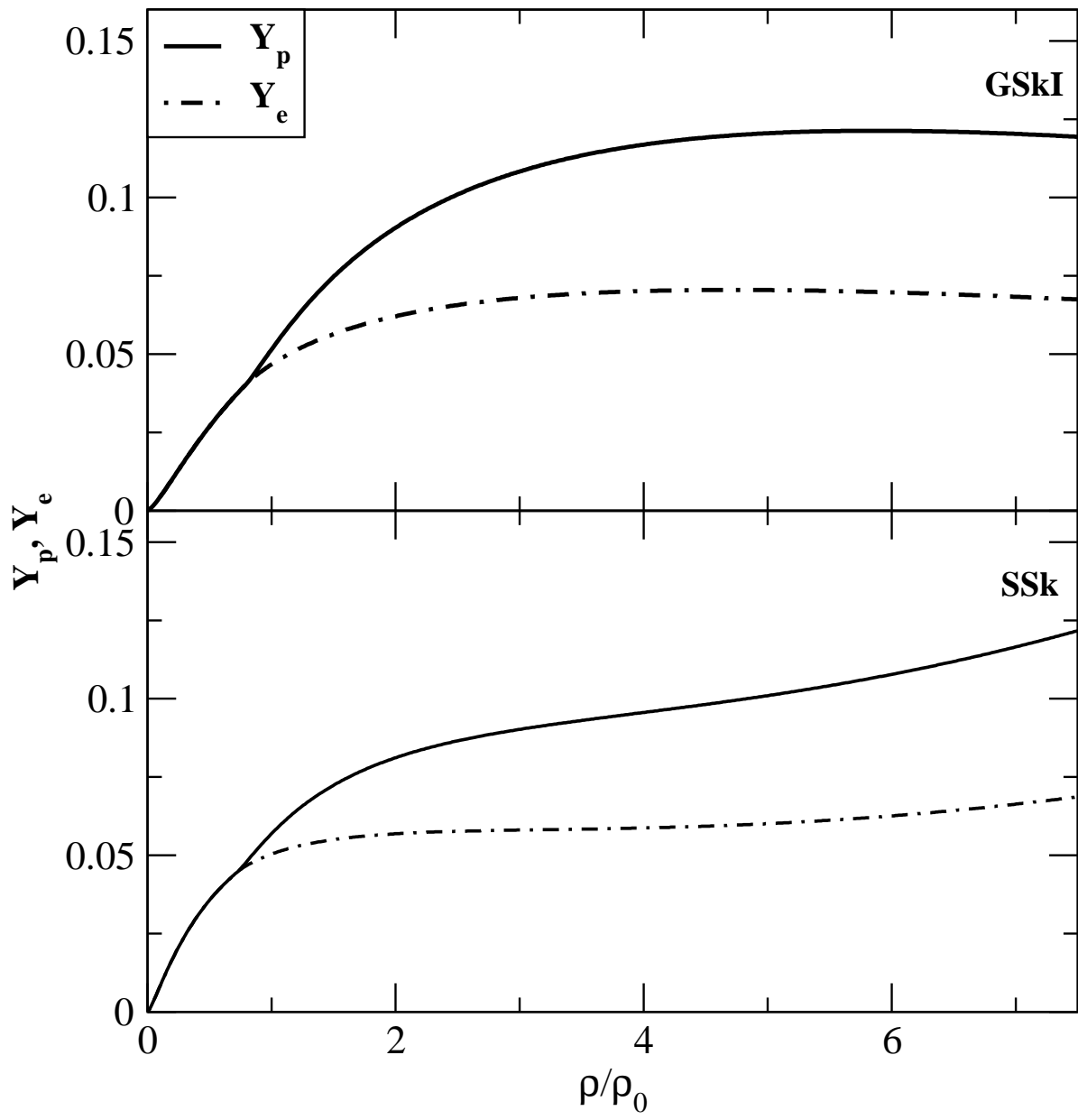


Fig. 8

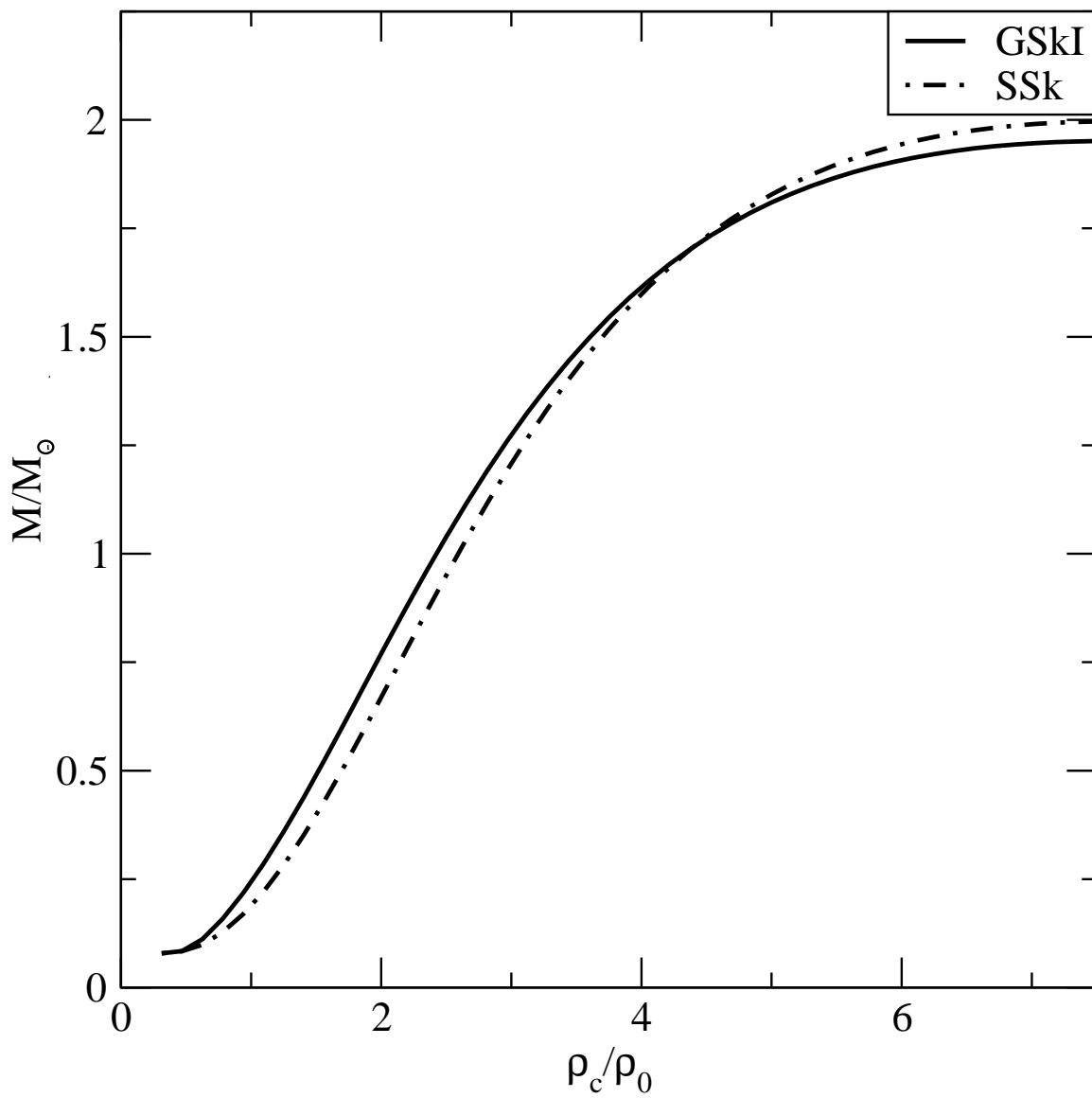


Fig. 9

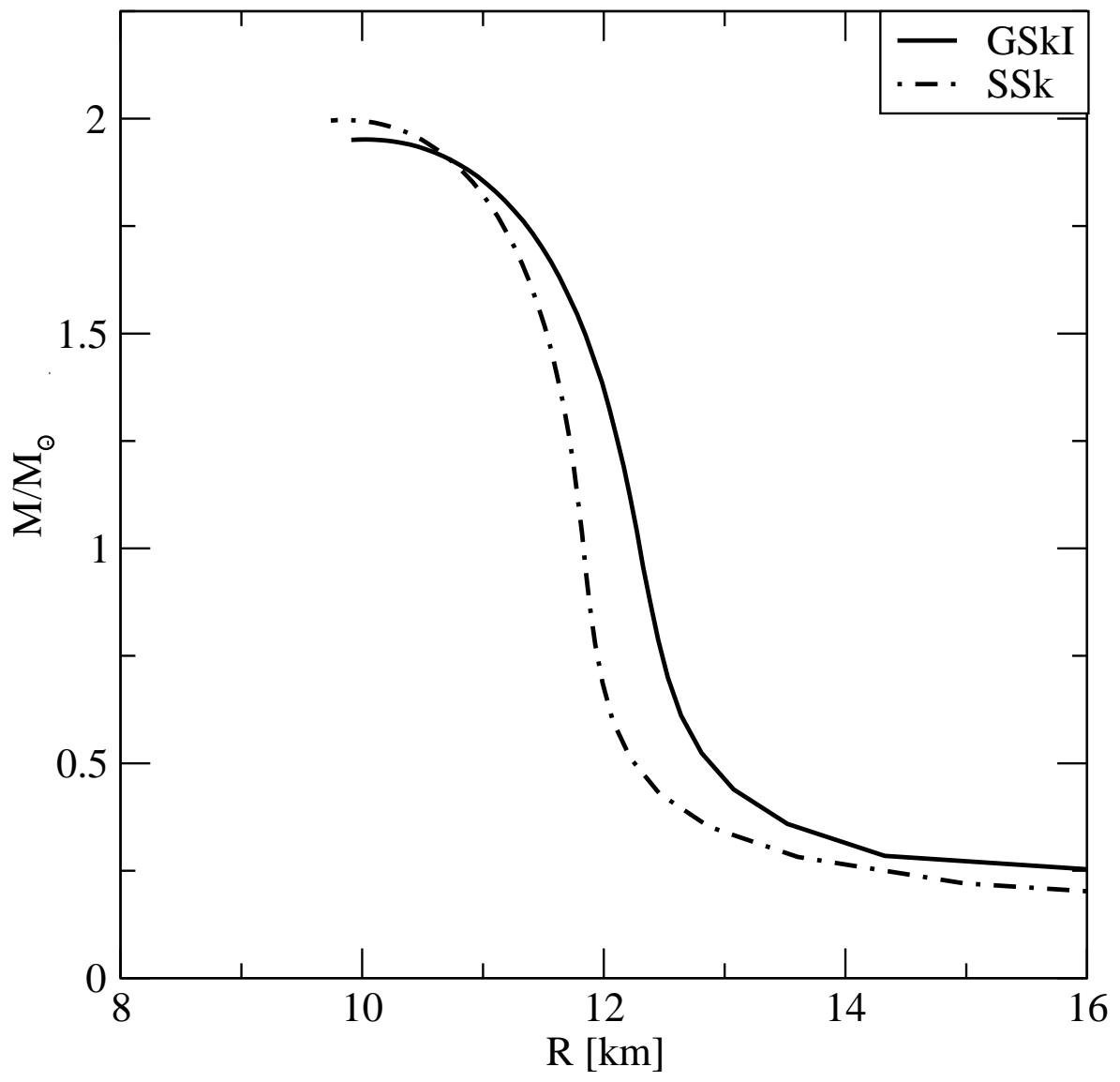


Fig. 10

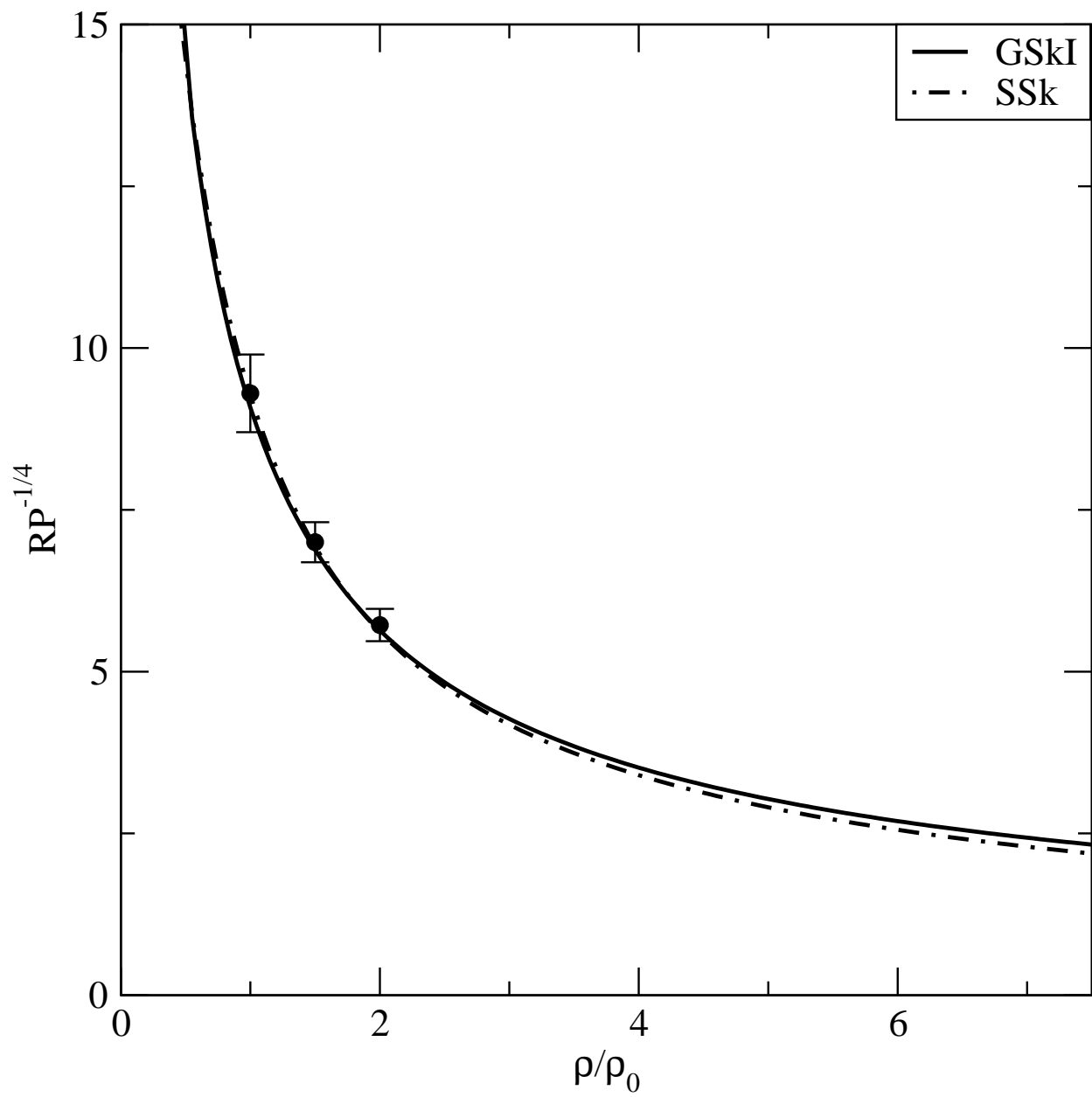


Fig. 11

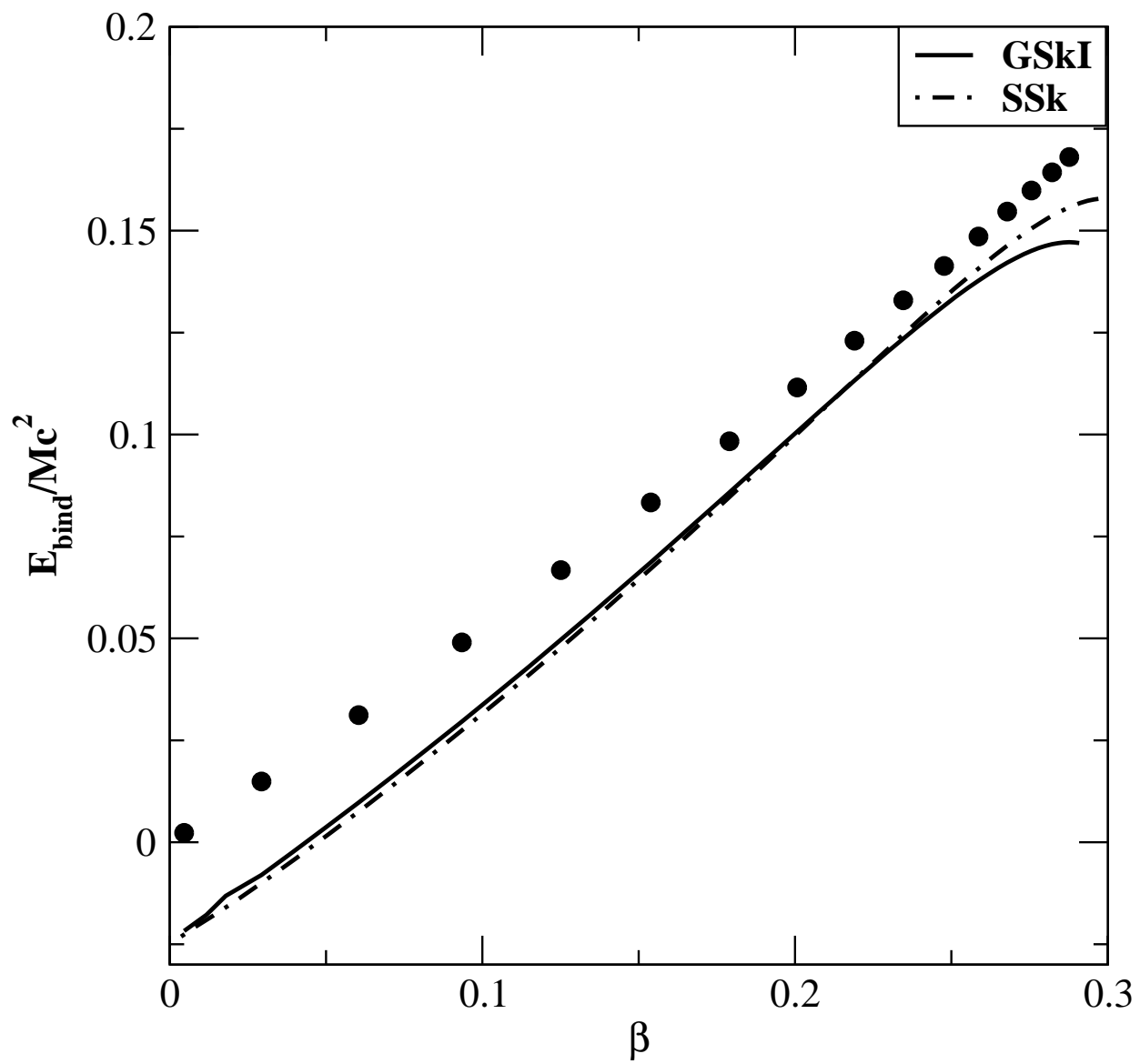


Fig. 12

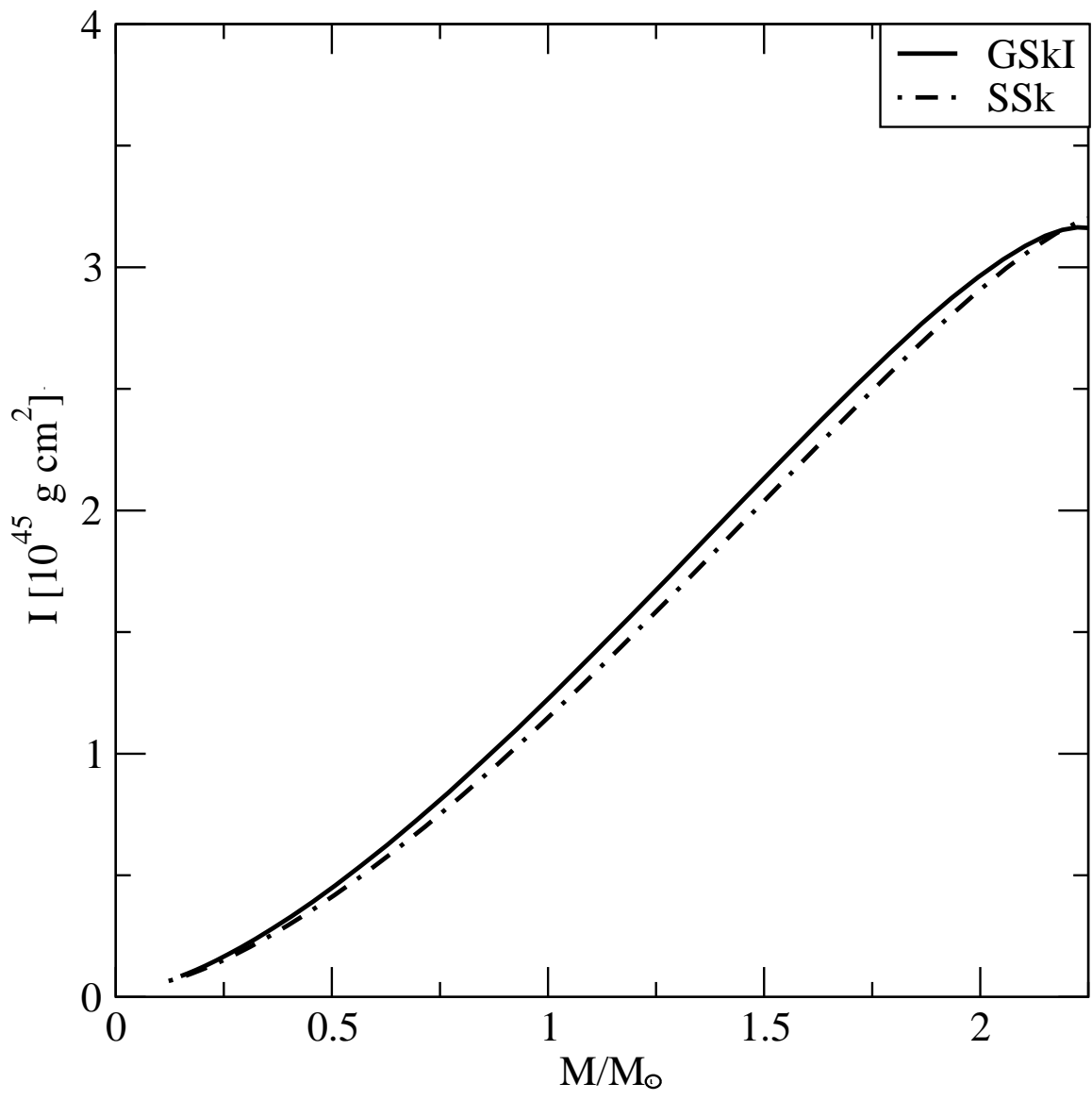


Fig. 13